for the health and function of the CNS (Hawkins and Davis 2005; Zlokovic 2008). Pericytes are vascular smooth muscle lineage cells that wrap around brain microvascular endothelial cells and share the basal membrane with endothelial cells. They are embedded in the basal lamina, which is composed of collagen type IV, laminin, and other extracellular matrix proteins (Farkas and Luiten 2001). There is heterogeneity in the relationship between pericytes and endothelial cells in different tissues. The pericyte coverage around microvessels is high in the brain (Shepro and Morel 1993; Allt and Lawrenson 2001). It is not clear why the brain requires vascular coverage with a high density of pericytes. Recently, pericytes have been found to augment BBB functions in cultured brain endothelial cells (Dohgu et al. 2005; Takata et al. 2007; Nakagawa et al. 2007). Although pericytes play a fundamental role in stabilizing brain capillary structure in vivo (Hellstrom et al. 2001), little is known about the role of pericytes in BBB functions in vivo.

Lipopolysaccharide (LPS), a major cell wall component of gram-negative bacteria, is known to be the main mediator of the high morbidity and mortality rates in septic shock (Titheradge 1999). Administration of high doses of LPS induces robust inflammatory responses that can result in septic shock. Sepsis is an acute systemic illness and a serious disorder with high rates of mortality. Much is known about the harmful effects of sepsis on peripheral organs such as lung, heart, liver, and kidney. However, the effects of sepsis on the brain are less clear. Septic encephalopathy has been reported to occur in the majority of septic patients (Young et al. 1990). Substantial loss of neurons was observed in the hippocampus of a rodent model of sepsis, resulting in significant residual behavioral deficits even after recovery from the sepsis (Semmler et al. 2007). BBB dysfunction has been shown in a rodent model of sepsis and in septic encephalopathy in human patients (Clawson et al. 1966; Jeppson et al. 1981; Deng et al. 1995; Young et al. 1992). We designed the present morphological study to examine the role of brain pericytes in the mediation of BBB disruption in an LPS-induced model of septic encephalopathy in mice. We provide the first evidence demonstrating that pericyte detachment from the basal lamina and microglial activation appear in parallel with cerebrovascular endothelial hyperpermeability in the hippocampus due to inflammatory responses to LPS.

Materials and Methods

Animals

Male ICR mice aged 8 weeks (Kyudo, Tosu, Japan) were housed at a temperature of 22 ± 2°C with a 12 h light/dark schedule (light on at 07:00 h) and given water and rat chow ad libitum. All the procedures involving experimental animals adhered to the law (No. 105) and notification (No. 6) of the Japanese Government, and were approved by the Laboratory Animal Care and Use Committee of Fukuoka University.

Animals were injected intraperitoneally with 20 mg/kg of bacterial lipopolysaccharide (*Escherichia coli* serotype 055:B5; SIGMA, St Louis, MO) in sterile physiological saline. Control groups received sterile physiological saline. The mortality rates induced by LPS (20 mg/kg) were 0, 10, and 25% at 3, 6, and 24 h after injection, respectively. The surviving mice at each time point were supplied for the experiments.

Immunohistochemical Procedures

At 1, 3, 6, and 24 h after saline or LPS injection, mice were anesthetized with sodium pentobarbital and then transcardially perfused with 4% paraformaldehyde in 0.1 M phosphate buffer (pH 7.4). The brains were subsequently removed, postfixed overnight at 4°C in 4% paraformaldehyde, and cryoprotected at 4°C in 30% sucrose until they sank. The brains were frozen in isopentane (−25°C) and stored at −80°C. Coronal sections (10 μm thickness) of the hippocampus were prepared on a cryostat (Leica CM1850, Leica Microsystems Nussloch GmbH, Nussloch, Germany) from approximately bregma −1.82 to −2.06 mm of the Paxinos and Franklin mouse brain atlas (2001).

The sections were washed in tris-buffered saline (TBS; pH 7.4) containing 0.2% Triton X-100 (0.2% Triton–TBS), background was blocked with blocking buffer (0.2% Triton–TBS containing 1% bovine serum albumin) at room temperature (RT), and then the sections were incubated overnight with anti-Iba1 antibody (Wako Pure Chemical Industries, Osaka,

Japan). Anti-Iba1 antibody was visualized with the DAKO EnVision® System-HRP (Dako North America Inc., Carpinteria, CA), counterstained with hematoxylin. The number of microglia was counted manually in three selected non-overlapping areas (400 × 400 μm^2) of CA1, CA2 -3, and dentate gyrus in the hippocampus. Three to five animals were used at each time point, and the numbers obtained from two to three sections were averaged in each animal.

For double staining of α-smooth muscle actin (αSMA) (a marker for pericytes) and laminin (a marker for the basal lamina), the sections were washed in 0.2% Triton–TBS. For antigen retrieval, sections were heated for 15 min at 121°C in an autoclave in 0.01 M sodium citrate (pH 6.0) and were then kept at RT for 20 min. The sections were washed in 0.2% Triton–TBS, background was blocked with blocking buffer at RT, then the sections were incubated overnight with mouse anti-αSMA antibody (ASM-1, PROGEN Biotechnik GmbH, Heidelberg, Germany) and rabbit anti-laminin antibody (SIGMA, St. Louis, MO). After incubation with primary antibodies, the sections were further incubated for 1 h at RT with Cy3-conjugated anti-rabbit IgG (1:500 dilution, Jackson ImmunoResearch, West Grove, PA) and fluorescein isothiocyanate (FITC)-conjugated anti-mouse IgG (1:200 dilution, Jackson ImmunoResearch). To evaluate cerebrovascular permeability at 24 h after LPS injection using double staining of CD31 antibody (a marker for endothelial cells) and fibrinogen, the sections were washed with 0.2% Triton–TBS, and background was blocked with blocking buffer at RT. The sections were incubated overnight with rat anti-CD31 antibody (BD Biosciences, San Jose, CA) and rabbit anti-fibrinogen antibody (Dako, North America Inc.). After incubation with primary antibodies, the sections were further incubated for 1 h at RT with Cy3-conjugated anti-rat IgG (1:200 dilution, Jackson ImmunoResearch) and FITC-conjugated anti-rabbit IgG (1:100 dilution, Jackson ImmunoResearch). The sections were mounted in the anti-fading medium VECTASHIELD mounting medium with DAPI (VECTOR Laboratories, Burlingame, CA), and then inspected using a fluorescence microscope (KEYENCE BZ-8000, KEYENCE Corporation, Osaka, Japan). Control sections were prepared by omission of primary antibodies or by mismatching secondary antibodies. Either method provided only weak non-specific staining.

Quantitative Measurements of Cerebrovascular Endothelial Permeability

Two hundred microliters of sodium fluorescein (Na–F) (Sigma) (6 mg/ml) was injected through the tail vein at 1, 3, 6, and 24 h after intraperitoneal injection of LPS or saline. Mice were anesthetized and then perfused with PBS 30 min after Na–F injection. The brains were quickly removed. The hippocampus was dissected and weighed. To assess fluorescence of Na–F, the samples were homogenized in 0.5 M borate buffer (pH 10) and centrifuged at 1,000×g for 15 min at 4°C. The supernatant (150 μl) was mixed with 150 μl of ethanol to precipitate proteins and then centrifuged (15,000×g) for 20 min at 4°C. The fluorescence concentration in the supernatant was determined by a CytoFluor Series 4000 fluorescence multiwell plate reader (PerSeptive Biosystems, Framingham, MA) using a fluorescent filter pair [Ex(λ) 485 ± 10 nm; Em(λ) 530 ± 12.5 nm]. The tissue content of Na–F was quantified from linear standard curves for Na–F.

Statistical Analysis

Values are expressed as the mean ± S.E.M. Statistical analysis was performed using two-way analysis of variance (ANOVA) followed by Bonferroni's post hoc test for multiple comparisons. The differences between the means were considered to be significant at $P < 0.05$.

Results

BBB Impairment after LPS Treatment

Cerebrovascular permeability was assessed by measurement of Na–F content in the hippocampus of LPS-treated mice. The accumulation of Na–F increased with time after LPS injection (Fig. 1A). Two-way ANOVA showed significant effects for the factors treatment (Saline and LPS) [$F(1, 31) = 30.91$, $P < 0.001$], time [$F(4, 31) = 12.42$, $P < 0.001$], and interaction (treatment × time) [$F(4, 31) = 8.971$, $P < 0.001$]. Bonferroni's post hoc test indicated that the accumulation of Na–F at 6 and 24 h after LPS injection was significantly increased when compared with samples that received saline injection at the same time points. Endogenous fibrinogen extravasation was

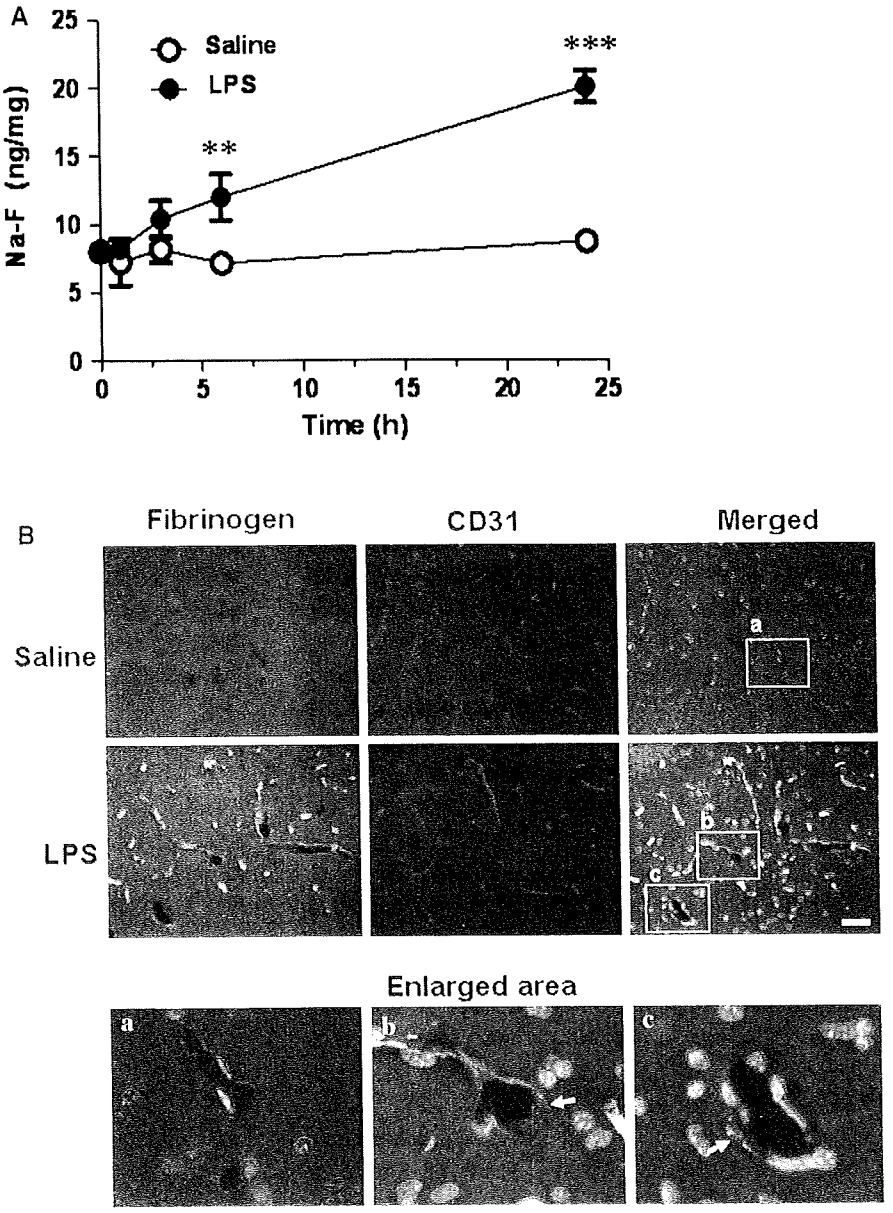

Fig. 1 BBB impairment in the hippocampus of LPS-induced sepsis in mice. **A** Time-course of Na–F accumulation in the hippocampus after saline or LPS injection. Values are the means ± S.E.M. ($n = 3$–5). $^{**}P < 0.01$, $^{***}P < 0.001$, significantly different from saline-treated mice. **B** Double immunofluorescence staining of fibrinogen (*green*) and CD31 (*red*) in the hippocampus 24 h after saline or LPS injection. Nuclei in the cells were stained with DAPI (*blue*). The enlarged photographs in the bottom panel (a, b, and c) represent the corresponding area indicated in the merged images (Saline (a) and LPS (b and c)). Arrows in the bottom panel indicate extravasation of fibrinogen. Scale bars = 50 μm

evaluated in the hippocampus 24 h after LPS injection (Fig. 1B). As shown in the bottom panels of Fig. 1B, fibrinogen staining was clearly detected around microvessels stained with anti-CD31 antibody in LPS-treated mice (Fig. 1B (b, c)) but not in saline-treated mice (Fig. 1B (a)).

Microglial Activation after LPS Treatment

We investigated morphological changes in microglia stained with anti-Iba1 antibody in the hippocampus after saline or LPS injection (Fig. 2A). Microglia in non-treated mice and saline-treated mice were observed with ramified thin processes and weak Iba1 staining, consistent with resting microglia (Fig. 2A (a, f)). The morphology of microglia in LPS-treated mice showed enlarged cytoplasm and cell bodies, irregular shape, and intensified Iba1 staining. This is characteristic of activated microglia (Fig. 2A (b–e)). The number of activated microglia increased with time after LPS injection. These morphological changes in microglia were not observed 1–24 h after saline

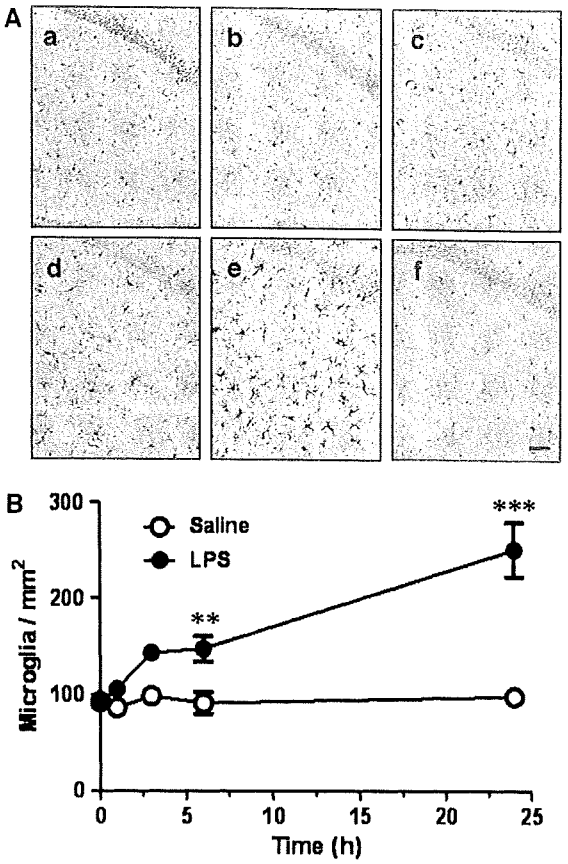

Fig. 2 Microglial activation in the hippocampus of LPS-induced sepsis in mice. **A** A series of photographs showing microglia in the hippocampus were taken at 0 (before) (a), 1 (b), 3 (c), 6 (d), and 24 h (e) after LPS injection and 24 h after saline injection (f). Brain sections were immunostained with anti-Iba1 antibody (an antibody specific to microglia). Scale bars = 50 μm. **B** Time-course of the number of microglia in the hippocampus in saline- or LPS-treated mice. The number of Iba1-positive microglia was averaged from three selected areas in the hippocampus. Values are the means ± S.E.M. (n = 3–5). $^{**}P < 0.01$, $^{***}P < 0.001$, significantly different from saline-treated mice

injection. A representative photograph of the hippocampus obtained 24 h after saline injection is shown in Fig. 2, panel A (f). As shown in Fig. 2B, the number of Iba1-positive microglia increased with time after LPS injection; this time-dependent increase was highly correlated with the time-course of the increased Na–F permeability (Fig. 1A). Two-way ANOVA showed significant effects for the factors treatment (Saline and LPS) [$F(1, 24) = 50.49, P < 0.001$], time [$F(4, 24) = 14.38, P < 0.001$], and interaction (treatment × time) [$F(4, 24) = 11.77, P < 0.001$] (Fig. 2B).

Structural Alterations in the Pericyte and Basal Lamina Unit after LPS Treatment

We observed morphological changes in pericytes and the basal lamina in the hippocampus of mice injected with LPS or saline (Fig. 3). In saline-treated mice, the whole pericyte was surrounded by basal lamina. These circular pericytes are expected to be wrapped around endothelial cells, although our immunohistochemical procedures are incapable of detecting both pericytes and endothelial cells in the same section. This is characteristic of normal brain microvascular structure (Fig. 3A, Saline). Morphological changes in pericytes were not observed 1 and 3 h after LPS injection. Six hours after injection, a broken part of basal lamina and detachment of pericytes from the basal lamina were detected, as shown in panels A and B (a, b) of Fig. 3. These changes were much apparent 24 h after LPS injection (Fig. 3A and B (c, d)). In LPS-treated mice, disorganization of the pericyte and basal lamina unit appeared in parallel with BBB impairment (Fig. 1) and microglial activation (Fig. 2).

Discussion

In the present study of LPS-induced sepsis in mice, cerebrovascular permeability to Na–F in the hippocampus increased with time from 1 to 24 h after LPS injection (Fig. 1A). This BBB dysfunction was supported by histochemical observations indicating the apparent extravasation of endogenous fibrinogen from microvessels (Fig. 1B). Microglia in the hippocampus were activated by LPS treatment, with the time-course of activation being consistent with increased cerebrovascular permeability (Fig. 2). An impairment of the basal lamina and detachment of pericytes from the basal lamina were detected in the hippocampus of LPS-treated mice (Fig. 3). The extent of these morphological changes in pericytes and the basal lamina correlated with increased microglial activation and increased cerebrovascular permeability. These findings suggest that pericyte detachment and microglial activation may be involved in the mediation of BBB disruption due to inflammatory responses to LPS.

Pericytes cover a major part of the abluminal endothelial surface and make contact with capillary

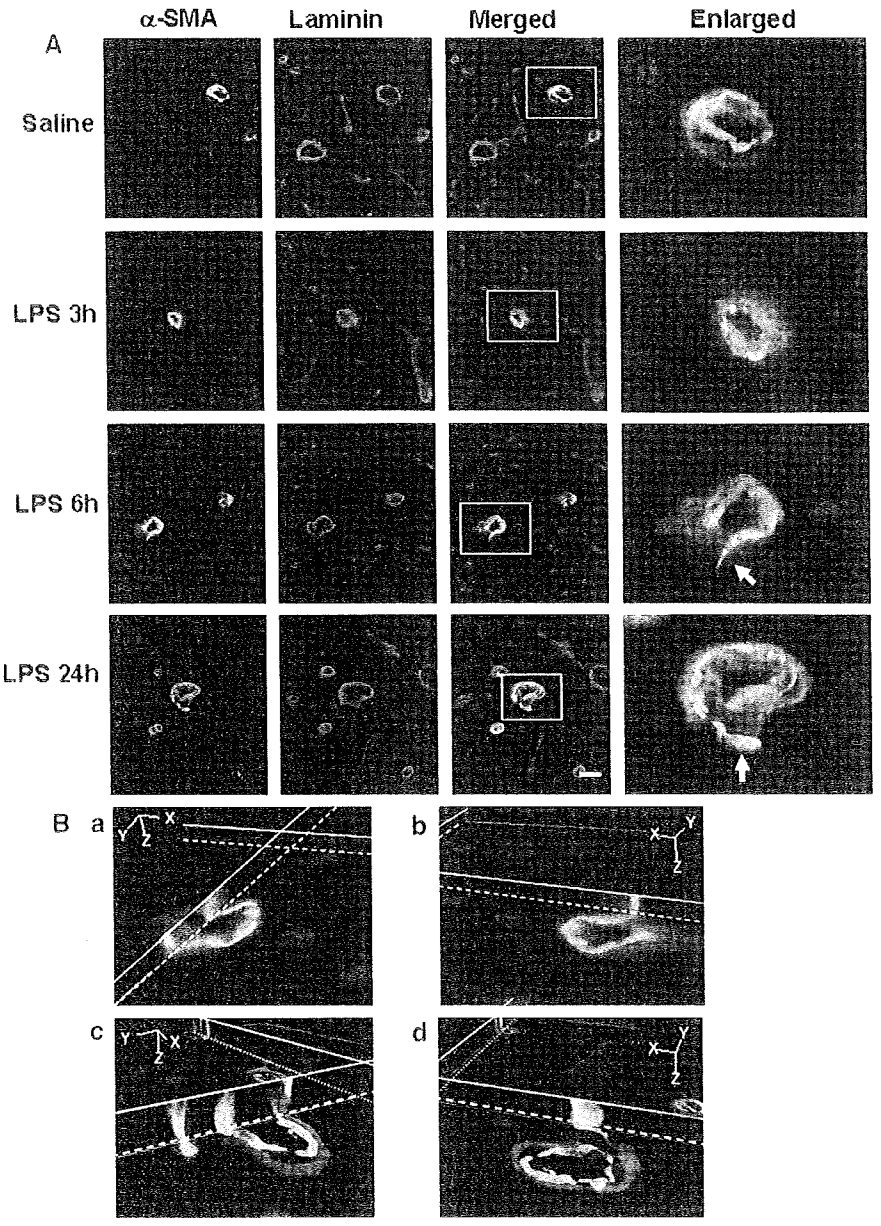

Fig. 3 Structural disorganization in the pericyte and basal lamina unit after LPS treatment. **A** Double immunofluorescence staining of α-SMA (*green*) and laminin (*red*) in the hippocampus 24 h after saline injection and 3, 6, and 24 h after LPS injection. Nuclei in the cells were stained with DAPI (*blue*). Boxed areas on the merged image (Merged) are enlarged in the fourth column (Enlarged) in panel **A**. Arrows show structural disorganization of the pericyte and basal lamina unit. Scale bars = 20 μm. **B** Three-dimensional reconstruction of the merged images are shown in panel **B**, 6 (a and b) and 24 h (c and d) after LPS injection. Image processing and three-dimensional images were assembled using KEYENCE BZ-Analyzer software. Each image is shown with a BZ-Analyzer-assisted orthogonal display. Two orthogonal planes (X–Z/Y–Z) are shown within the three-dimensional images

endothelial cells via gap junctions, adhesion plaques, and peg-and-socket junctions (Rucker et al. 2000). Pericytes are important for control of the growth and migration of endothelial cells and contribute to vascular stability (Ramsauer et al. 2002). Several ligand–receptor systems including transforming growth factor (TGF)-β/TGF-β receptor and platelet-derived growth factor (PDGF)-B/PDGF receptor β (PDGFR-β) have been implicated in the regulation of vascular stability through pericyte and endothelial cell interactions (von Tell et al. 2006). We reported that continuous TGF-β production in brain pericytes is attributed to pericyte-induced induction and up-regulation of the BBB (Dohgu et al. 2005). On the other hand, in PDGF-B- and PDGFR-β-deficient mice, the primary cause of the phenotype was lack of pericytes (Lindahl et al. 1997; Crosby et al. 1998). These knockout mice showed various pathological conditions accompanied by pericyte loss: endothelial hyperplasia, increased capillary diameter, abnormal vascular morphogenesis, changes in the cellular distribution of certain junctional proteins, and

morphological signs of increased endothelial permeability (Hellstrom et al. 2001). Pericytes express toll-like receptor-4 (TLR-4), which is up-regulated by LPS (Edelman et al. 2006). Pericytes, when exposed to LPS, produce proinflammatory cytokines through TLR-4 and this is involved in the capillary leakage observed in acute lung injury in sepsis (Edelman et al. 2007a; Edelman et al. 2007b). It is therefore likely that LPS may cause pericyte detachment from the basal lamina by directly activating pericytes through TLR-4. These findings support the present study demonstrating that structural disorganization of the pericyte and basal lamina unit is attributable to BBB impairment in LPS-induced sepsis in mice. Receptors on pericytes including TGF-β receptor, PDGFR-β, and TLR-4 may participate in this process.

In the human diabetic retina, pericyte loss is a hallmark of early changes (Cogan et al. 1961). Experimental hyperglycemia enhances detachment of retinal pericytes, leading to reduced pericyte coverage of retinal capillaries and reduced inhibition of endothelial proliferation (Hammes et al. 2002). Brain pericyte detachment and migration from vessels into the perivascular parenchyma are demonstrated after brain ischemia or traumatic brain injury (Dore-Duffy et al. 2000; Gonul et al. 2002; Melgar et al. 2005). Pericytes regulate brain capillary blood flow by contraction and relaxation (Peppiatt et al. 2006). Cerebral blood flow is decreased in patients with septic encephalopathy (Maekawa et al. 1991). Based on these findings concerning pericyte behavior in pathological conditions, pericytes are highly likely to play a key role in maintaining the physiological functions of neurovascular units including the blood–retinal barrier and BBB.

It has been shown that microglial activation is increased in sepsis patients (Lemstra et al. 2007). Activated microglia migrate to lesion foci and release matrix metalloproteinases and cytokines. In particular, metalloproteinase release and activation cause BBB impairment by degrading the basal lamina (Gursoy-Ozdemir et al. 2004; Gurney et al. 2006). BBB disruption provokes the immediate and focal activation of microglia (Nimmerjahn et al. 2005). In multiple sclerosis, BBB disruption permits the leakage of fibrinogen into brain, and then fibrinogen activates microglia via the Mac-1 integrin receptor (Adams et al. 2007). Together with this evidence, the present findings suggest that microglial activation induced by BBB impairment may facilitate disorganization in the pericyte and basal lamina unit due to proteolytic digestion of the basal lamina, leading to aggravation of the BBB impairment.

In conclusion, we suggest that pericyte detachment from the basal lamina and microglial activation could mediate BBB impairment due to inflammatory responses in the damaged brain. Our findings highlight brain pericytes as a key factor in modulating functions of neurovascular units including the BBB.

Acknowledgments This work was supported in part by Grants-in-Aid for Scientific Research [(B) 17390159], Grants-in-Aid for Young Scientists [(Start-up) 18890227], Grants-in-Aid for Young Scientists [(B) 19790199] from JSPS, Japan, the Ministry of Health, Labor and Welfare of Japan (H19-nanchi-ippan-006), the Nakatomi Foundation and Research Foundation ITSUU Laboratory. The authors thank Dr. Mária A. Deli (Institute of Biophysics, Biological Research Centre of the Hungarian Academy of Sciences) for pertinent comments on the manuscript and Ms. Hiromi Nakanishi for technical assistance.

References

Adams RA, Bauer J, Flick MJ, Sikorski SL, Nuriel T, Lassmann H, Degen JL, Akassoglou K (2007) The fibrin-derived gamma377–395 peptide inhibits microglia activation and suppresses relapsing paralysis in central nervous system autoimmune disease. J Exp Med 204(3):571–582. doi:10.1084/jem.20061931

Allt G, Lawrenson JG (2001) Pericytes: cell biology and pathology. Cells Tissues Organs 169(1):1–11. doi:10.1159/000047855

Clawson CC, Hartmann JF, Vernier RL (1966) Electron microscopy of the effect of gram-negative endotoxin on the blood–brain barrier. J Comp Neurol 127:183–198. doi:10.1002/cne.901270204

Cogan DG, Toussaint D, Kuwabara T (1961) Retinal vascular patterns. IV. Diabetic retinopathy. Arch Ophthalmol 66:366–378

Crosby JR, Seifert RA, Soriano P, Bowen-Pope DF (1998) Chimaeric analysis reveals role of Pdgf receptors in all muscle lineages. Nat Genet 18(4):385–388. doi:10.1038/ng0498-385

Deng X, Wang X, Anderrson R (1995) Endothelial barrier resistance in multiple organs after septic and nonseptic challenges in the rat. J Appl Physiol 78:2052–2061

Dohgu S, Takata F, Yamauchi A, Nakagawa S, Egawa T, Naito M, Tsuruo T, Sawada Y, Niwa M, Kataoka Y (2005) Brain pericytes contribute to the induction and up-regulation of blood-brain barrier functions through transforming growth factor-beta production. Brain Res 1038:208–215. doi:10.1016/j.brainres.2005.01.027

Dore-Duffy P, Owen C, Balabanov R, Murphy S, Beaumont T, Rafols JA (2000) Pericyte migration from the vascular

wall in response to traumatic brain injury. Microvasc Res 60(1):55–69. doi:10.1006/mvre.2000.2244

Edelman DA, Jiang Y, Tyburski J, Wilson RF, Steffes C (2006) Toll-like receptor-4 message is up-regulated in lipopolysaccharide-exposed rat lung pericytes. J Surg Res 134(1):22–27. doi:10.1016/j.jss.2006.03.007

Edelman DA, Jiang Y, Tyburski JG, Wilson RF, Steffes CP (2007a) Cytokine production in lipopolysaccharide-exposed rat lung pericytes. J Trauma 62(1):89–93. doi:10.1097/TA.0b013e31802dd712

Edelman DA, Jiang Y, Tyburski JG, Wilson RF, Steffes CP (2007b) Lipopolysaccharide activation of pericyte's Toll-like receptor-4 regulates co-culture permeability. Am J Surg 193(6):730–735. doi:10.1016/j.amjsurg.2006.08.086

Farkas E, Luiten PG (2001) Cerebral microvascular pathology in aging and Alzheimer's disease. Prog Neurobiol 64(6):575–611. doi:10.1016/S0301-0082(00)00068-X

Gonul E, Duz B, Kahraman S, Kayali H, Kubar A, Timurkaynak E (2002) Early pericyte response to brain hypoxia in cats: an ultrastructural study. Microvasc Res 64(1):116–119. doi:10.1006/mvre.2002.2413

Gurney KJ, Estrada EY, Rosenberg GA (2006) Blood-brain barrier disruption by stromelysin-1 facilitates neutrophil infiltration in neuroinflammation. Neurobiol Dis 23(1):87–96. doi:10.1016/j.nbd.2006.02.006

Gursoy-Ozdemir Y, Qiu J, Matsuoka N, Bolay H, Bermpohl D, Jin H, Wang X, Rosenberg GA, Lo EH, Moskowitz MA (2004) Cortical spreading depression activates and upregulates MMP-9. J Clin Invest 113(10):1447–1455

Hammes HP, Lin J, Renner O, Shani M, Lundqvist A, Betsholtz C, Brownlee M, Deutsch U (2002) Pericytes and the pathogenesis of diabetic retinopathy. Diabetes 51(10):3107–3112. doi:10.2337/diabetes.51.10.3107

Hawkins BT, Davis TP (2005) The blood-brain barrier/neurovascular unit in health and disease. Pharmacol Rev 57(2):173–185. doi:10.1124/pr.57.2.4

Hellstrom M, Gerhardt H, Kalen M, Li X, Eriksson U, Wolburg H, Betsholtz C (2001) Lack of pericytes leads to endothelial hyperplasia and abnormal vascular morphogenesis. J Cell Biol 153:543–553. doi:10.1083/jcb.153.3.543

Jeppson B, Freund HR, Gimmon Z, James JH, von Meyenfeldt MF, Fischer JE (1981) Blood–brain barrier derangement in sepsis: cause of septic encephalopathy? Am J Surg 141:136–141. doi:10.1016/0002-9610(81)90026-X

Lemstra AW, Groen in't Woud JC, Hoozemans JJ, van Haastert ES, Rozemuller AJ, Eikelenboom P, van Gool WA (2007) Microglia activation in sepsis: a case-control study. J Neuroinflammation 4:4. doi:10.1186/1742-2094-4-4

Lindahl P, Johansson BR, Levéen P, Betsholtz C (1997) Pericyte loss and microaneurysm formation in PDGF-B-deficient mice. Science 277(5323):242–245. doi:10.1126/science.277.5323.242

Löscher W, Potschka H (2005) Drug resistance in brain diseases and the role of drug efflux transporters. Nat Rev Neurosci 6(8):591–602. doi:10.1038/nrn1728

Maekawa T, Fujii Y, Sadamitsu D, Yokota K, Soejima Y, Ishikawa T, Miyauchi Y, Takeshita H (1991) Cerebral circulation and metabolism in patients with septic encephalopathy. Am J Emerg Med 9(2):139–143. doi:10.1016/0735-6757(91)90175-J

Melgar MA, Rafols J, Gloss D, Diaz FG (2005) Postischemic reperfusion: ultrastructural blood-brain barrier and hemodynamic correlative changes in an awake model of transient forebrain ischemia. Neurosurgery 56(3):571–581. doi:10.1227/01.NEU.0000154702.23664.3D

Nakagawa S, Deli MA, Nakao S, Honda M, Hayashi K, Nakaoke R, Kataoka Y, Niwa M (2007) Pericytes from brain microvessels strengthen the barrier integrity in primary cultures of rat brain endothelial cells. Cell Mol Neurobiol 27(6):687–694. doi:10.1007/s10571-007-9195-4

Nimmerjahn A, Kirchhoff F, Helmchen F (2005) Resting microglial cells are highly dynamic surveillants of brain parenchyma in vivo. Science 308(5726):1314–1318. doi:10.1126/science.1110647

Paxinos G, Franklin KBJ (2001) The mouse brain in stereotaxic coordinates. Academic Press, San Diego

Peppiatt CM, Howarth C, Mobbs P, Attwell D (2006) Bidirectional control of CNS capillary diameter by pericytes. Nature 443(7112):700–704. doi:10.1038/nature05193

Ramsauer M, Krause D, Dermietzel R (2002) Angiogenesis of the blood-brain barrier in vitro and the function of cerebral pericytes. FASEB J 16(10):1274–1276

Rucker HK, Wynder HJ, Thomas WE (2000) Cellular mechanisms of CNS pericytes. Brain Res Bull 51(5):363–369. doi:10.1016/S0361-9230(99)00260-9

Semmler A, Frisch C, Debeir T, Ramanathan M, Okulla T, Klockgether T, Heneka MT (2007) Long-term cognitive impairment, neuronal loss and reduced cortical cholinergic innervation after recovery from sepsis in a rodent model. Exp Neurol 204(2):733–740. doi:10.1016/j.expneurol.2007.01.003

Shepro D, Morel NM (1993) Pericyte physiology. FASEB J 7(11):1031–1038

Takata F, Dohgu S, Yamauchi A, Sumi N, Nakagawa S, Naito M, Tsuruo T, Shuto H, Kataoka Y (2007) Inhibition of transforming growth factor-beta production in brain pericytes contributes to cyclosporin A-induced dysfunction of the blood-brain barrier. Cell Mol Neurobiol 27(3):317–328. doi:10.1007/s10571-006-9125-x

Titheradge MA (1999) Nitric oxide in septic shock. Biochim Biophys Acta 1411(2–3):437–455. doi:10.1016/S0005-2728(99)00031-6

von Tell D, Armulik A, Betsholtz C (2006) Pericytes and vascular stability. Exp Cell Res 312(5):623–629. doi:10.1016/j.yexcr.2005.10.019

Young GB, Bolton CF, Austin TW, Archibald YM, Gonder J, Wells GA (1990) The encephalopathy associated with septic illness. Clin Invest Med 13(6):297–304

Young GB, Bolton CF, Archibald YM, Austin TW, Wells GA (1992) The electroencephalogram in sepsis-associated encephalopathy. J Clin Neurophysiol 9(1):145–152. doi:10.1097/00004691-199201000-00016

Zlokovic BV (2008) The blood-brain barrier in health and chronic neurodegenerative disorders. Neuron 57(2):178–201. doi:10.1016/j.neuron.2008.01.003

Neuroscience Letters 449 (2009) 71–75

Contents lists available at ScienceDirect

Neuroscience Letters

journal homepage: www.elsevier.com/locate/neulet

Adrenomedullin-induced relaxation of rat brain pericytes is related to the reduced phosphorylation of myosin light chain through the cAMP/PKA signaling pathway

Fuyuko Takata[a,d], Shinya Dohgu[a], Tsuyoshi Nishioku[a], Hiroyuki Takahashi[a], Eriko Harada[a], Ikuko Makino[b], Manabu Nakashima[c], Atsushi Yamauchi[a], Yasufumi Kataoka[a,d,*]

[a] Department of Pharmaceutical Care and Health Sciences, Faculty of Pharmaceutical Sciences, Fukuoka University, Fukuoka, Japan
[b] Department of Obstetrics and Gynecology, Tokyo Women's Medical University Medical Center East, Tokyo, Japan
[c] Department of Immunological and Molecular Pharmacology, Faculty of Pharmaceutical Sciences, Fukuoka University, Fukuoka, Japan
[d] BBB Laboratory, PharmaCo-Cell Co., Ltd., Nagasaki, Japan

ARTICLE INFO

Article history:
Received 21 August 2008
Received in revised form 16 October 2008
Accepted 23 October 2008

Keywords:
Brain pericytes
Adrenomedullin
Myosin light chain
Relaxation
cAMP
Protein kinase A

ABSTRACT

Brain pericytes are known to embrace the abluminal endothelial surfaces of cerebral microvessels. The rich expression of contractile proteins in these cells suggests pericytal regulation of cerebral blood flow. Here, we investigated the molecular mechanisms by which an endothelium-derived relaxing factor, adrenomedullin, was able to induce the relaxation of rat primary cultured brain pericytes. Adrenomedullin increased the relative proportion of pericytes that were relaxed, as shown by an increased cell surface area. A smaller fragment of adrenomedullin (adrenomedullin$_{22-52}$) blocked the adrenomedullin-induced relaxation. Adrenomedullin increased intracellular cAMP concentrations and decreased the phosphorylation of myosin light chain (MLC). H89 (a PKA inhibitor) inhibited the adrenomedullin-induced increase in the number of relaxed pericytes, and returned the level of phosphorylation of MLC to the control level. The results of the present study suggest that adrenomedullin-induced relaxation of brain pericytes is related to the reduced phosphorylation of MLC through cAMP/PKA.

Pericytes are located adjacent to the capillaries and share a common basement membrane with endothelial cells. They are important for the growth and migration of endothelial cells and the integrity of microvascular capillaries [21,26]. Pericytes reside on the microvasculature where smooth muscle is lacking. In the brain, the capillary wall is comprised of brain microvessel endothelial cells and brain pericytes. Given their intimate association with vessels and their morphology, it had been suggested that they may serve in a contractile capacity similar to the smooth muscle cells of larger vessels [22]. Because pericytes have abundant contractile filaments, such as α-smooth muscle actin [1], the contraction of brain pericytes has been postulated to regulate the cerebral microcirculation. In fact, vasoactive compounds, such as acetylcholine, noradrenaline, phenylephrine [18], endothelin-1, and serotonin [9], induced contraction of cultured brain pericytes. Recently, it was reported that the brain capillary diameter was bidirectionally controlled by pericytes [20]. Thus, brain pericytes are assumed to regulate cerebral blood flow in response to various vasoactive agents. Brain pericytes possess the contractile proteins α-smooth muscle actin, a muscle-specific form of actin [1], and muscle-specific isoforms of myosin [5], similar to the smooth muscle cells. Contraction and relaxation of the smooth muscle are regulated by phosphorylation/dephosphorylation of Ser19 on the 20-kDa regulatory light chain of myosin (MLC). Therefore, the dephosphorylation of MLC might induce relaxation of brain pericytes as well as smooth muscle cells.

Adrenomedullin has been established as an important secretory product of the vascular endothelium, since the discovery that adrenomedullin gene expression is 20–40-fold higher in endothelial cells than in the adrenal medulla [24]. Adrenomedullin, a peptide involved in cerebrovascular disease [16], induces increases in cerebral blood flow [3]. Brain endothelial cells are a potential source of adrenomedullin in the brain [12]. Adrenomedullin acts through a receptor component known as calcitonin receptor-like receptor (CRLR), the activity of which is modified by specific proteins known as receptor activity-modifying proteins (RAMPs). When CRLR is coupled to RAMP-2 or RAMP-3, the receptor binds predominantly to adrenomedullin [15]. Brain pericytes

* Corresponding author at: Department of Pharmaceutical Care and Health Sciences, Faculty of Pharmaceutical Sciences, Fukuoka University, 8-19-1 Nanakuma, Jonan-ku, Fukuoka, Japan. Tel.: +81 92 862 2696; fax: +81 92 862 2699.
E-mail address: ykataoka@fukuoka-u.ac.jp (Y. Kataoka).

0304-3940/$ – see front matter © 2008 Elsevier Ireland Ltd. All rights reserved.
doi:10.1016/j.neulet.2008.10.082

express adrenomedullin receptor components, which are potential targets of endothelial-derived adrenomedullin [12]. A role of adrenomedullin in contractile properties of pericytes remains unclear.

Here, we demonstrate that adrenomedullin induces relaxation of rat brain pericytes and that this phenomenon is related to the reduced phosphorylation of MLC through cAMP/protein kinase A (PKA)-dependent mechanisms.

Adrenomedullin, adrenomedullin$_{22-52}$ and 8-(4-chlorophenylthio)-cyclic AMP were obtained from Sigma (St. Louis, MO, USA). H89 and Ro 20-1724 were obtained from D. Western Therapeutics Institute (Nagoya, Japan) and Calbiochem (San Diego, CA), respectively. All remaining reagents of analytical grade were purchased from Wako (Osaka, Japan), unless otherwise indicated.

Brain pericytes were isolated from 3-week-old Wistar rats, according to the method of Hayashi et al. [6]. Briefly, cerebral cortices were minced and incubated with collagenase CLS2 (1 mg/mL; Worthington, Lakewood, NJ). After neurons and glial cells were removed by centrifugation in 20% bovine serum albumin (BSA)–DMEM, the pellets were further digested with collagenase/dispase (1 mg/mL; Roche, Mannheim, Germany). The microvessel clusters in the pellet were separated on a 33% Percoll gradient. The obtained brain microvessel fragments were placed in uncoated culture flasks in DMEM supplemented with 20% FBS (FBS–DMEM), 100 units/mL penicillin, and 100 μg/mL streptomycin. After 7 days in culture, rat pericytes overgrew brain endothelial cells and typically reached 80–90% confluency. Cells at the second passage were used for experiments. All procedures involving experimental animals adhered to the law (No. 105) and notification (No.6) of the Japanese Government, and were approved by the Laboratory Animal Care and Use Committee of Fukuoka University.

Rat brain pericytes (10,000 cells/cm^2) were seeded onto center-well organ culture dishes (1.77 cm in diameter, BD FALCON™, BD Biosciences, NJ). After 1 day in culture, a dish was placed on the stage of a light microscope equipped with a digital camera (BZ-8000; KEYENCE, Osaka) at 37 °C with a humidified atmosphere of 5% CO_2/95% air. To initiate morphological observations, pericytes were incubated with 300 μl of 20% FBS–DMEM. After a 30-min period of pre-incubation, the medium was removed and cells were exposed to 2% BSA in Krebs–Ringer buffer (118 mM NaCl, 4.7 mM KCl, 2.6 mM $CaCl_2$, 1.2 mM $MgCl_2$, 1.0 mM NaH_2PO_4, 25 mM $NaHCO_3$, and 11 mM D-glucose, pH 7.4) containing various testing reagents. The several places in a dish were sequentially photographed before and 10, 20 and 30 min after exposure of cells to various reagents. Morphological changes in pericytes were evaluated by calculating the surface area of each cell using real-time 3D analysis software accompanying the BZ-8000 system (KEYENCE). Several places in a dish were selected at random; then, approximately 40 pericytes in total obtained from the selected places were monitored for calculation of cell surface area. Based on the changes in cell surface area, we categorized the pericytes into three subtypes as follows: (1) relaxed pericytes (RPs), defined as pericytes showing a >10% increase in basal cell surface area in response to the reagent; (2) contracted pericytes (CPs), defined as pericytes showing a >10% decrease in basal cell area in response to the reagent; and (3) unchanged pericytes (UPs), defined as pericytes showing a <10% change in basal area in response to the reagent. Measurement of cell surface areas was performed by three observers blind to treatments. The intraobserver and interobserver variations for measurement of cell surface areas were <5% in each experiment. Results are expressed as the percentages of measured pericytes from each dish that were classed as RPs, CPs and UPs.

Changes in the cellular cAMP concentrations of rat brain pericytes (5.0×10^4 cells/cm^2) after exposure to 1 and 10 μM adrenomedullin for 30 min at 37 °C were measured using an enzyme immunoassay (cAMP Biotrak Enzyme Immunoassay System, GE Healthcare UK Ltd., Bucks., UK).

After treatment with vehicle (control), adrenomedullin (10 μM) or adrenomedullin (10 μM) plus H89 (1 μM) for 30 min at 37 °C, brain pericytes were lysed in a buffer containing 60 mM *n*-octyl-β-D-glucopyranoside, 0.5% NP-40, 50 mM HEPES, 500 mM NaCl, 10% glycerol, 20 mM Na_3VO_4, 50 mM NaF, 10 mM $Na_4O_7P_2 \cdot 10H_2O$, 50 ng/mL phenyl-methylsulfonyl fluoride, phosphatase inhibitor cocktail 1 (Sigma), phosphatase inhibitor cocktail 2 (Sigma) and protease inhibitor cocktail (Sigma). The total protein concentration in cell lysates was determined using a BCA Protein assay kit (PIERCE, Rockford, IL). Equivalent amounts of each protein sample were electrophoretically separated on 4–20% SDS-polyacrylamide gels (Daiichi Pure Chemicals Co., Ltd.; Tokyo, Japan) and transferred to polyvinylidene difluoride membranes. Rabbit polyclonal anti-phospho-Ser-19 of MLC, rabbit polyclonal anti-MLC or mouse monoclonal GAPDH antibodies were used according to the manufacturer's recommendations. The results were visualized using an ECL Advance Western Blotting Detection Kit (GE Healthcare UK Ltd, Bucks). Densitometric analysis was performed using a FluorChem SP imaging system with AlphaEaseFC software (Alpha Innotech, CA). The expression level of GAPDH was employed to normalize that of MLC or p-MLC.

The percentages of the three response types among all cells (RPs, CPs and UPs) were analyzed by the Kruskal–Wallis rank test to assess the significant differences among groups. Comparisons between two treatment groups were performed using the Mann–Whitney *U*-test. Other data are expressed as means with S.E.M. The statistical significance of differences between groups was assessed by one-way analysis of variance (ANOVA) for factorial comparisons and by Tukey–Kramer's test for multiple comparisons. Differences were considered significant when P values were less than 0.05.

To test whether adrenomedullin induces relaxation of the rat brain pericytes, the effects of adrenomedullin on the percentage of three response types of brain pericytes (RPs, CPs and UPs) were examined. In preliminary experiments, brain pericytes showed no significant differences in the relative proportions of RPs, CPs and UPs among batches obtained from separate cultures (data not shown). Adrenomedullin (10 μM) increased the relative proportion of RPs with time during the period 10–30 min after treatment (Fig. 1B). A 30-min exposure to adrenomedullin (10 μM) increased the relative proportion of RPs from 12.5% to 50%, although 1 μM adrenomedullin produced no effect (Fig. 1A). There were no changes in the relative proportion of CPs after various treatments. Then, brain pericytes were treated with 10 μM adrenomedullin for 30 min (Fig. 1C). When brain pericytes were treated with adrenomedullin$_{22-52}$, an adrenomedullin receptor antagonist, adrenomedullin (10 μM) failed to produce a significant change in the relative proportions of the three response types of brain pericytes (Fig. 1D). Adrenomedullin$_{22-52}$ (10 and 40 μM) inhibited the adrenomedullin-induced increase in the relative proportion of RPs.

Adrenomedullin (1 and 10 μM) increased cAMP levels over those in control pericytes (75.2 ± 10.5 and 136.5 ± 6.5 fmol/well, respectively (n = 3–4)) (Fig. 2A). When cells were exposed to 8-(4-chlorophenylthio)-cyclic AMP (250 and 500 μM; a cAMP stable analogue) and Ro 20-1724 (17.5 μM; a cAMP-specific phosphodiesterase IV inhibitor), the cAMP analogue increased the relative proportion of RPs (Fig. 2B). Subsequently, we examined the effect of H89 (a PKA-specific inhibitor) on adrenomedullin-induced relaxation of brain pericytes (Fig. 2C). H89 (0.1 and 1 μM) inhibited the adrenomedullin-induced increase in the relative proportion of RPs.

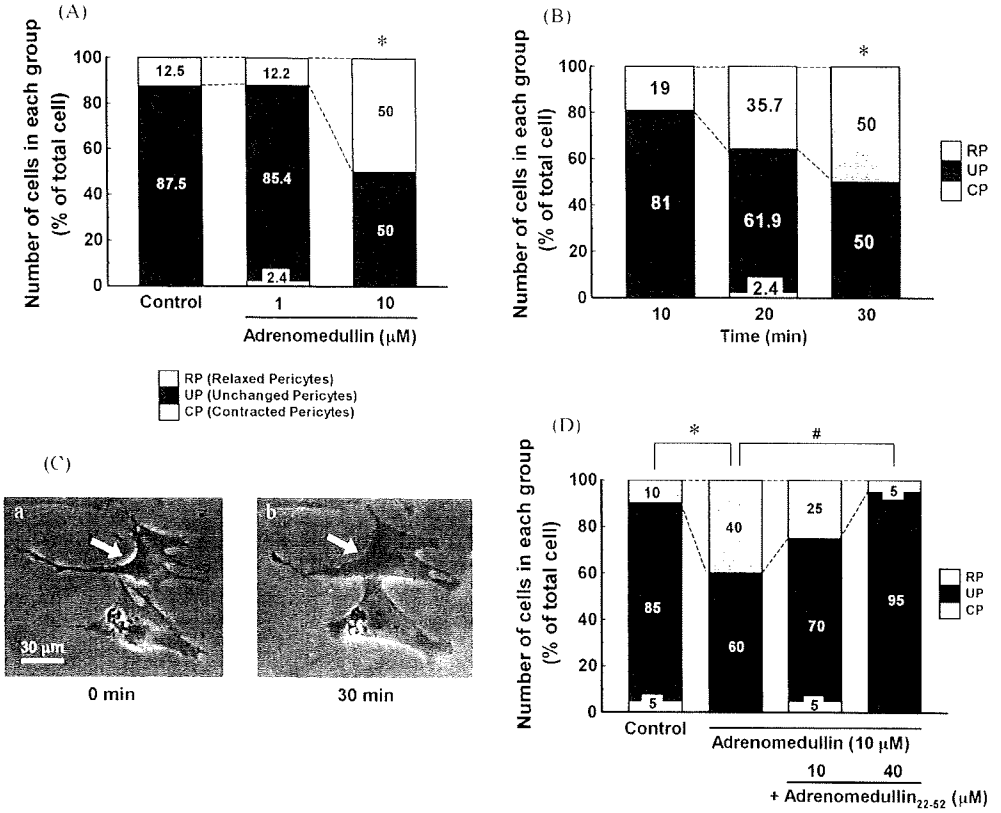

Fig. 1. (A) Percentages of three response types of brain pericytes exposed to adrenomedullin. (B) Time-course of the percentages of three response types of brain pericytes during 10–30 min after addition of adrenomedullin (10 μM). RP, UP, and CP indicate relaxed, unchanged, and contracted pericytes, respectively. The numeral shown in each column indicates the relative proportion of each response type of brain pericytes. (C) Representative morphological changes of brain pericytes just before (0 min) (a) and 30 min after addition of adrenomedullin (10 μM) (b). (D) Percentages of three response types of brain pericytes exposed to adrenomedullin with adrenomedullin$_{22-52}$. $^{*}p < 0.05$, significant difference from control. $^{\#}p < 0.05$, significant difference from adrenomedullin treatment.

To test whether phosphorylation of MLC is involved in adrenomedullin-induced relaxation of brain pericytes, we examined the effect of adrenomedullin on the phosphorylation of MLC by Western blot analysis (Fig. 3). Adrenomedullin (10 μM) significantly decreased p-MLC/MLC ratios in brain pericytes to 76.5 ± 7.0% of the control ratio. This decrease reversed to control levels in the presence of H89 (1 μM). When pericytes were treated with H89 (1 μM), the ratio of p-MLC/total MLC was almost the same as that in vehicle-treated cells (control) (104.0 ± 0.7% of control, $n = 3$).

Accumulating evidence from studies using various methods suggest that brain pericytes possess contractile properties and regulate cerebral microvascular blood flow in response to various vasoactive agents [18,20]. However, the intracellular machinery involved in the regulation of contractile properties remains obscure, whereas brain pericytes express contractile proteins similar to smooth muscle cells [1]. To assess the contractility of brain pericytes grown on culture dishes, we intended to establish a new assay based on real-time morphological observation of the alterations of cell surface area using a phase-contrast microscope equipped with a CO_2 incubator. We confirmed that some brain pericytes extended their surface areas in response to adrenomedullin (Fig. 1C). We also found that brain pericytes expressed MLC, and that adrenomedullin reduced the levels of phosphorylated MLC. These findings suggest a correlation between the changes in cell surface area and the contractile properties.

Adrenomedullin receptors are coupled to adenylate cyclase and their stimulation leads to a marked raise in cAMP levels, the second messenger that mediates the cellular actions of adrenomedullin [8,10]. We demonstrated that stimulation of brain pericytes with adrenomedullin induced an increase in cAMP levels and that cAMP had adrenomedullin-like effects on pericytes (Fig. 2A, B). Inhibition of PKA by H89 also reduced adrenomedullin-induced relaxation of pericytes (Fig. 2C). These data provide evidence for the involvement of cAMP-dependent PKA in mediating adrenomedullin-induced relaxation of pericytes as the intracellular signaling pathway.

The levels of phosphorylation of MLC at Ser-19 primarily determine contraction and relaxation in smooth muscle. MLC phosphorylation promotes smooth muscle contraction, whereas p-MLC dephosphorylation results in muscle relaxation [27]. In the present study, adrenomedullin enhanced dephosphorylation of p-MLC, this phenomenon being reduced by the inhibition of PKA by H89 (Fig. 3). In addition to demonstrating that brain pericytes are relaxed by adrenomedullin, we found that these cells also possess MLC, similar to smooth muscle cells. Therefore, reduced phosphorylation levels of MLC provably contribute to the relaxation of brain pericytes by adrenomedullin. The phosphorylation of MLC is regulated by two enzymes: MLC kinase (MLCK), a Ca^{2+}/calmodulin-dependent protein kinase, and MLC phosphatase (MLCP). In smooth muscle cells, these two enzymes are regulated by PKA. An increase in PKA activity could result from increases in cellular cAMP [4], which are associated with MLCK phosphorylation [14]. PKA phosphorylates MLCK at Ser-512 resulting in a decrease in the affinity of MLCK for Ca^{2+}/calmodulin [2]. PKA phosphorylates Ser-695 of myosin

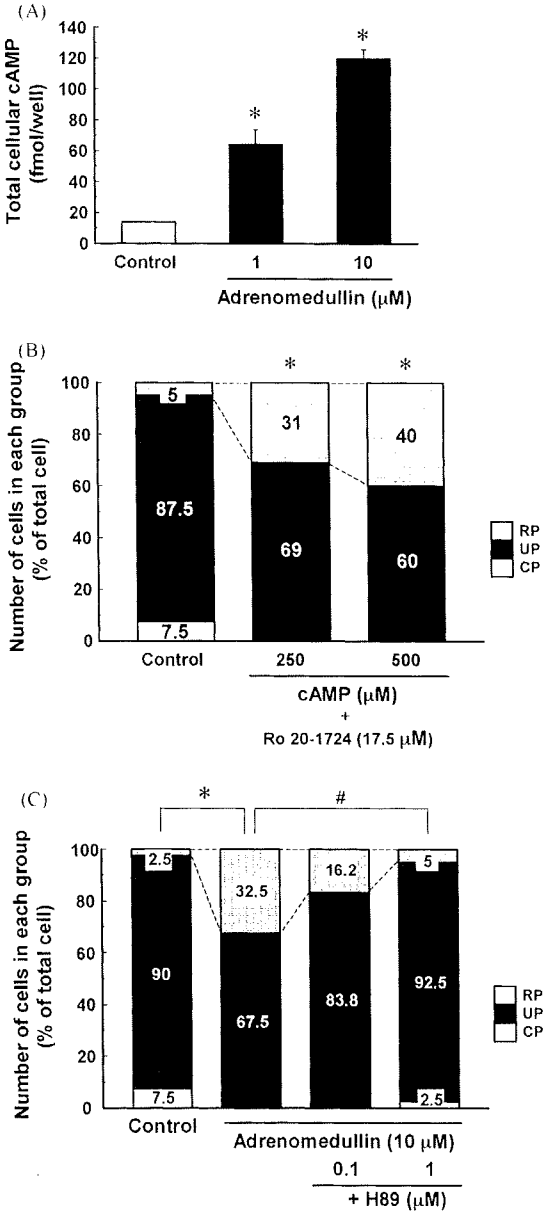

Fig. 2. (A) Effect of adrenomedullin on cellular levels of cAMP in brain pericytes. Values are the means ± S.E.M. ($n = 3$–4). *$p < 0.05$, significant differences from control. (B and C) Percentages of three response types of brain pericytes exposed to cAMP with Ro 20-1724 (B) or adrenomedullin with or without H89 (C). RP, UP, and CP indicate relaxed, unchanged, and contracted pericytes, respectively. The numeral shown in each column indicates the relative proportion of each response type of the cells. *$p < 0.05$, significant difference from control. #$p < 0.05$, significant difference from adrenomedullin treatment.

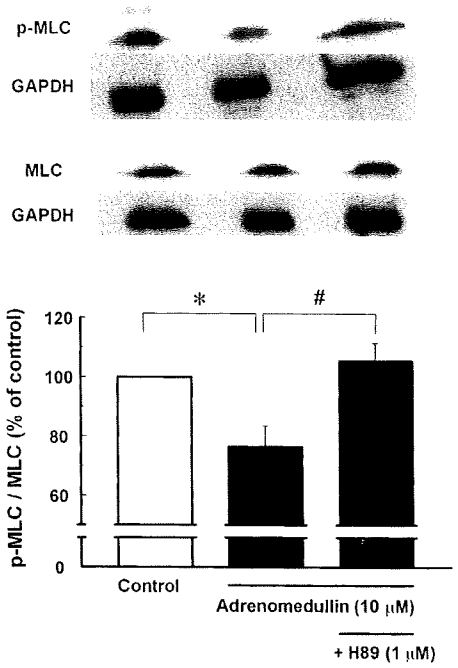

Fig. 3. Effect of adrenomedullin on phosphorylation levels of MLC in brain pericytes. Brain pericytes were exposed to adrenomedullin with or without H89. The top panel indicates a representative Western blot of MLC, p-MLC and each corresponding GAPDH. The bottom columns show p-MLC/MLC ratio expressed as a percentage of the control ratio. The ratios of p-MLC/MLC in control cells were 0.49, 0.62, and 1.02 in three separate experiments. Values are means ± S.E.M. *$p < 0.05$, significant difference from control. #$p < 0.05$, significant difference from adrenomedullin.

phosphatase-targeting subunit 1 (MYTP1), resulting in an increase in MLCP activity through inhibition of phosphorylation of Thr-696 by MYTP1 kinase [17,28]. Thus, it is conceivable that both inhibition of MLCK and activation of MLCP through PKA activation induced by adrenomedullin may lead to reduced phosphorylation of MLC in brain pericytes.

In the present study, we classified 50–60% of brain pericytes as UPs after adrenomedullin treatment. A lack of response of some pericytes was observed in previous findings of pericytes in brain capillaries [20]. In smooth muscle cells and fibroblasts, the level of α-smooth muscle actin is known to be related to their level of contractile force generation [7,23]. In addition to the expression of myosin, that of α-smooth muscle actin in pericytes could indicate that pericytes function in the control of blood flow [1,13,22]. Earlier studies have demonstrated that cultured vascular smooth muscle cells undergo differential expression of α-smooth muscle actin in relation to their growth state [19]. Therefore, the presence of responder and non-responder pericytes exposed to adrenomedullin may be due to the heterogenous growth state. Further studies are required to clarify this point.

In conclusion, we demonstrated that adrenomedullin induced the relaxation of rat brain pericytes. Our results suggested that adrenomedullin induces relaxation of pericytes and that this phenomenon is related to the reduced phosphorylation of MLC through the cAMP/PKA pathway. The vasodilator effect of adrenomedullin in the cerebral circulation is supported by several observations in different species [11] and adrenomedullin induces increases in cerebral blood flow [3,25]. Thus, the facilitatory effects of adrenomedullin on cerebral microvascular circulation may be attributable to the relaxation of brain pericytes.

Acknowledgments

This work was supported, in part, by Grants-in-Aid for Scientific Research [(B) 17390159], Grants-in-Aid for Young Scientists [(Start-up) 18890227], Grants-in-Aid for Young Scientists [(B) 19790199] from JSPS, Japan and the Ministry of Health, Labor and Welfare of Japan (H19-nanchi-ippan-006), Research Foundation ITSUU Laboratory and Global FU Program Grant from Fukuoka University. The authors would like to thank Ms. Sachiyo Hashiguchi for her technical help.

References

[1] R. Bandopadhyay, C. Orte, J.G. Lawrenson, A.R. Reid, S. De Silva, G. Allt, Contractile proteins in pericytes at the blood–brain and blood–retinal barriers, J. Neurocytol. 30 (2001) 35–44.

[2] M.A. Conti, R.S. Adelstein, The relationship between calmodulin binding and phosphorylation of smooth muscle myosin kinase by the catalytic subunit of 3′:5′ cAMP-dependent protein kinase, J. Biol. Chem. 256 (1981) 3178–3181.

[3] A. Dogan, Y. Suzuki, N. Koketsu, K. Osuka, K. Saito, M. Takayasu, M. Shibuya, J. Yoshida, Intravenous infusion of adrenomedullin and increase in regional cerebral blood flow and prevention of ischemic brain injury after middle cerebral artery occlusion in rats, J. Cereb. Blood Flow. Metab. 17 (1997) 19–25.

[4] A. Eckly-Michel, V. Martin, C. Lugnier, Involvement of cyclic nucleotide-dependent protein kinases in cyclic AMP-mediated vasorelaxation, Br. J. Pharmacol. 122 (1997) 158–164.

[5] E. Ehler, G. Karlhuber, H.C. Bauer, A. Draeger, Heterogeneity of smooth muscle-associated proteins in mammalian brain microvasculature, Cell. Tissue Res. 279 (1995) 393–403.

[6] K. Hayashi, S. Nakao, R. Nakaoke, S. Nakagawa, N. Kitagawa, M. Niwa, Effects of hypoxia on endothelial/pericytic co-culture model of the blood–brain barrier, Regul. Pept. 123 (2004) 77–83.

[7] B. Hinz, G. Celetta, J.J. Tomasek, G. Gabbiani, C. Chaponnier, Alpha-smooth muscle actin expression upregulates fibroblast contractile activity, Mol. Biol. Cell. 12 (2001) 2730–2741.

[8] Y. Ishizaka, Y. Ishizaka, M. Tanaka, K. Kitamura, K. Kangawa, N. Minamino, H. Matsuo, T. Eto, Adrenomedullin stimulates cyclic AMP formation in rat vascular smooth muscle cells, Biochem. Biophys. Res. Commun. 200 (1994) 642–646.

[9] M. Kamouchi, T. Kitazono, T. Ago, M. Wakisaka, H. Ooboshi, S. Ibayashi, M. Iida, Calcium influx pathways in rat CNS pericytes, Brain Res. Mol. Brain Res. 126 (2004) 114–120.

[10] J. Kato, K. Kitamura, K. Kangawa, T. Eto, Receptors for adrenomedullin in human vascular endothelial cells, Eur. J. Pharmacol. 289 (1995) 383–385.

[11] B. KisB, C.S. Abrahám, M.A. Deli, H. Kobayashi, A. Wada, M. Niwa, H. Yamashita, Y. Ueta, Adrenomedullin in the cerebral circulation, Peptides 22 (2001) 1825–1834.

[12] B. Kis, H. Kaiya, R. Nishi, M.A. Deli, C.S. Abrahám, T. Yanagita, T. Isse, S. Gotoh, H.H. Kobayashi, A. Wada, M. Niwa, K. Kangawa, J. Greenwood, H. Yamashita, Y. Ueta, Cerebral endothelial cells are a major source of adrenomedullin, J. Neuroendocrinol. 14 (2002) 283–293.

[13] C.H. Lai, K.H. Kuo, J.M. Leo, Critical role of actin in modulating BBB permeability, Brain Res. Brain Res. Rev. 50 (2005) 7–13.

[14] P. de Lanerolle, M. Nishikawa, D.A. Yost, R.S. Adelstein, Increased phosphorylation of myosin light chain kinase after an increase in cyclic AMP in intact smooth muscle, Science 223 (1984) 1415–1417.

[15] L.M. McLatchie, N.J. Fraser, M.J. Main, A. Wise, J. Brown, N. Thompson, R. Solari, M.G. MG, S.M. Foord, RAMPs regulate the transport and ligand specificity of the calcitonin-receptor-like receptor, Nature 393 (1998) 333–339.

[16] K. Miyashita, H. Itoh, H. Arai, T. Suganami, N. Sawada, Y. Fukunaga, M. Sone, K. Yamahara, T. Yurugi-Kobayashi, K. Park, N. Oyamada, N. Sawada, D. Taura, H. Tsujimoto, T.H. Chao, N. Tamura, M. Mukoyama, K. Nakao, The neuroprotective and vasculo-neuro-regenerative roles of adrenomedullin in ischemic brain and its therapeutic potential, Endocrinology 147 (2006) 1642–1653.

[17] K. Nakamura, Y. Koga, H. Sakai, K. Homma, M. Ikebe, cGMP-dependent relaxation of smooth muscle is coupled with the change in the phosphorylation of myosin phosphatase, Circ. Res. 101 (2007) 712–722.

[18] K. Oishi, T. Kamiyashiki, Y. Ito, Isometric contraction of microvascular pericytes from mouse brain parenchyma, Microvasc. Res. 73 (2007) 20–28.

[19] G.K. Owens, A. Loeb, D. Gordon, M.M. Thompson, Expression of smooth muscle-specific alpha-isoactin in cultured vascular smooth muscle cells: relationship between growth and cytodifferentiation, J. Cell. Biol. 102 (1986) 343–352.

[20] C.M. Peppiatt, C. Howarth, P. Mobbs, D. Attwell, Bidirectional control of CNS capillary diameter by pericytes, Nature 443 (2006) 700–704.

[21] M. Ramsauer, D. Krause, R. Dermietzel, Angiogenesis of the blood–brain barrier in vitro and the function of cerebral pericytes, FASEB J. 16 (2002) 1274–1276.

[22] H.K. Rucker, H.J. Wynder, W.E. Thomas, Cellular mechanisms of CNS pericytes, Brain Res. Bull. 51 (2000) 363–369.

[23] L.A. Schildmeyer, R. Braun, G. Taffet, M. Debiasi, A.E. Burns, A. Bradley, R.J. Schwartz, Impaired vascular contractility and blood pressure homeostasis in the smooth muscle alpha-actin null mouse, FASEB J. 14 (2000) 2213–2220.

[24] S. Sugo, N. Minamino, K. Kangawa, K. Miyamoto, K. Kitamura, J. Sakata, T. Eto, H. Matsuo, Endothelial cells actively synthesize and secrete adrenomedullin, Biochem. Biophys. Res. Commun. 201 (1994) 1160–1166.

[25] M. Takao, M. Tomita, N. Tanahashi, M. Kobari, Y. Fukuuchi, Transient vasodilatory effects of adrenomedullin on cerebral parenchymal microvessels in cats, Neurosci. Lett. 268 (1999) 147–150.

[26] W.E. Thomas, Brain macrophages: on the role of pericytes and perivascular cells, Brain Res. Brain Res. Rev. 31 (1999) 42–57.

[27] M.P. Walsh, The Ayerst Award Lecture 1990. Calcium-dependent mechanisms of regulation of smooth muscle contraction, Biochem. Cell. Biol. 69 (1991) 771–800.

[28] A.A. Wooldridge, J.A. MacDonald, F. Erdodi, C. Ma, M.A. Borman, D.J. Hartshorne, T.A. Haystead, Smooth muscle phosphatase is regulated in vivo by exclusion of phosphorylation of threonine 696 of MYPT1 by phosphorylation of Serine 695 in response to cyclic nucleotides, J. Biol. Chem. 279 (2004) 34496–34504.

Journal of the Neurological Sciences 285 (2009) 100–108

Contents lists available at ScienceDirect

Journal of the Neurological Sciences

journal homepage: www.elsevier.com/locate/jns

Comparison study of amyloid PET and voxel-based morphometry analysis in mild cognitive impairment and Alzheimer's disease

Masaaki Waragai [a], Nobuyuki Okamura [b,*], Katsutoshi Furukawa [a], Manabu Tashiro [c], Shozo Furumoto [b,d], Yoshihito Funaki [e], Motohisa Kato [b], Ren Iwata [e], Kazuhiko Yanai [b], Yukitsuka Kudo [f], Hiroyuki Arai [a]

[a] Department of Geriatrics and Gerontology, Division of Brain Sciences, Institute of Development, Aging and Cancer, Tohoku University, Sendai, Japan
[b] Department of Pharmacology, Tohoku University School of Medicine, Sendai, Japan
[c] Division of Cyclotron Nuclear Medicine, Cyclotron and Radioisotope Center, Tohoku University, Sendai, Japan
[d] Department of Nuclear Medicine and Radiology, Institute of Development, Aging and Cancer, Tohoku University, Sendai, Japan
[e] Division of Radiopharmaceutical Chemistry, Cyclotron and Radioisotope Center, Tohoku University, Sendai, Japan
[f] Innovation of New Biomedical Engineering Center, Tohoku University, Sendai, Japan

ARTICLE INFO

Article history:
Received 27 February 2009
Received in revised form 5 May 2009
Accepted 2 June 2009
Available online 23 June 2009

Keywords:
Alzheimer's disease
Amyloid
Early diagnosis
Magnetic resonance imaging
Positron emission tomography
BF-227

ABSTRACT

Two techniques employed for the early diagnosis of dementia are the imaging of amyloid-β protein using positron emission tomography (PET) and voxel-based morphometry analysis of MRI (VBM-MRI). The purpose of this study was to evaluate the clinical utility of amyloid PET and VBM-MRI for the early diagnosis and tracking of the severity of Alzheimer's disease (AD). The neuritic plaque burden and gray matter losses were evaluated using [^{11}C]BF-227-PET and VBM-MRI in 12 healthy controls, 13 subjects with mild cognitive impairment (MCI), including 6 who converted to AD and 7 who did not convert, and 15 AD patients. The AD patients and the MCI converters exhibited a neocortical retention of BF-227 and parahippocampal gray matter loss shown by VBM-MRI. The MCI converters were more clearly distinguished from the MCI non-converters in BF-227-PET than VBM-MRI. The combined sample of the MCI converters and AD patients showed a significant correlation of MMSE scores with the global gray matter loss, but not with the BF-227 retention. These findings suggest that amyloid PET using [^{11}C]BF-227 is better suited for the prediction of conversion from MCI to AD, while VBM-MRI appears to be better suited for tracking the severity of dementia.

1. Introduction

Alzheimer's disease (AD) is a neurodegenerative disorder characterized by a progressive impairment of cognitive function and behavior. AD is the most common form of dementia, particularly in the elderly [1,2]. The pathological hallmarks of AD are extracellular amyloid-β protein deposits called senile plaques (SPs) and intracellular neurofibrillary tangles (NFTs), which occur together with selective neuronal and synaptic loss [3,4]. These changes are also associated with progressive neuronal loss and resultant cerebral atrophy [5]. The presence of both SPs and NFTs are prerequisites for a definitive diagnosis of AD, but more attention has been focused on the role of amyloid-β protein (Aβ) in the pathogenesis of AD. Although the mechanisms of development of AD have not been completely elucidated, Aβ is assumed to play a causal role in the pathology of AD.

In vivo imaging techniques that can non-invasively and reliably assess Aβ deposition are currently receiving considerable attention in the search for a method for early diagnosis of AD [6–11]. Pittsburgh Compound-B (PIB) is at present the most commonly used probe for Aβ and has been applied to the diagnosis of AD and several other neurological disorders [12–16]. For example, amnesic mild cognitive impairment (MCI) is currently considered a prodromal state of AD, though not all individuals with MCI will develop AD; MCI converters and non-converters are difficult to distinguish from a clinical and neuropsychological perspective. Analysis of PIB-PET images in MCI subjects revealed a bimodal distribution of PIB uptake in the neocortex. About two thirds of MCI cases showed neocortical retention of PIB similar in distribution (and sometimes in degree) to AD, while the other third of MCI cases showed no cortical retention, similar to normal individuals [15,17,18]. A previous PIB-PET study demonstrated higher PIB retention in MCI converters than in non-converters, suggesting the utility of amyloid imaging in the prediction of progression to dementia [18].

We have developed novel benzoxazole derivatives for in vivo imaging of amyloid [19–21]. One of these agents, 2-(2-[2-demethylaminothiazol-5-yl]ethenyl)-6-(2-[Fluoro]ethoxy)benzoxazole (BF-227), displayed a high binding affinity to Aβ fibrils, excellent brain uptake and specifically labels amyloid deposits in transgenic mice [20,22]. A clinical PET study using [^{11}C]BF-227 demonstrated higher retention of this tracer in the

* Corresponding author. Department of Pharmacology, Tohoku University School of Medicine, Tohoku University, 2-1 Seiryo-machi, Aoba-ku, Sendai 980-8575, Japan. Tel.: +81 22 717 8058; fax: +81 22 717 8060.
E-mail address: oka@mail.tains.tohoku.ac.jp (N. Okamura).

0022-510X/$ – see front matter © 2009 Elsevier B.V. All rights reserved.
doi:10.1016/j.jns.2009.06.005

neocortex of AD patients than normal individuals [22]. There are several drawbacks to the use of this tracer, including its relatively low affinity to AD brain tissue ($K_d = 25$ nM) compared to PIB [23] and its slower clearance from the white matter region due to its higher lipophilicity (Log$P = 1.75$),[22] resulting in lower signal to background ratio than PIB–PET. However, the voxel-based analysis of BF-227–PET images indicated a pattern of tracer distribution distinct from that of PIB–PET.[12] Intriguingly, the preferential [^{11}C]BF-227 retention in the posterior neocortical region of the AD brain corresponded with an area containing a high density of neuritic plaques [4,22]. A preliminary report of the direct comparison of PIB–PET and BF-227–PET in the same AD patients additionally demonstrated a difference in the regional distribution of these two agents, which presumably reflects their different preference for various conformations of Aβ in the senile plaque generation process [24]. From these findings, we speculate that BF-227 detects neuritic plaques containing dense amyloid fibrils preferentially, compared to PIB–PET, and provides unique information about the Aβ pathology in AD patients. The early detection of Aβ deposition is important to begin medication to prevent a cognitive decline in the stage of MCI, since it appears that the deposition of Aβ starts earlier than the clinical diagnosis of dementia [25–27]. Approximately 20–30% of healthy, age-matched subjects exhibited neocortical retention of PIB, predominantly in the prefrontal and posterior cingulate cortices [15,16]. The demonstration of PIB retention in a proportion of normal individuals supports postmortem observations that Aβ aggregation predominantly occurs before the onset of dementia. However, there is currently no evidence that all PIB-positive normal individuals are destined to develop dementia. Highly sensitive detection of Aβ leads to a potential risk for misjudging the process of normal physiological aging as a pathological indicator of AD. The accurate prediction of AD progression is thus necessary to prevent the administration of non-essential treatments to individuals who are not at risk of converting to AD. In particular, a shift of brain Aβ from the soluble to fibrillar form is closely associated with onset of AD [28]. Thus, selective detection of dense amyloid fibrils would be advantageous to differentiate normal aging process from AD with high specificity, as the deposition of neuritic plaques is strongly associated with the earliest symptoms of AD [25]. Based on this background evidence, we anticipated that BF-227–PET would more accurately predict the conversion from MCI to AD than other imaging techniques.

Cognitive decline is reported to strongly correlate with cortical atrophy in AD, suggesting that cortical degeneration is the primary basis of cognitive decline in AD [5]. Thus, an increased rate of cerebral atrophy, as evaluated using MRI, is a diagnostic feature of AD that correlates with the clinical stage/severity and is thought to represent the macroscopic consequences of neuronal destruction [29–31]. Medial temporal lobe atrophy, as seen in MRI scans of AD patients, is a sensitive marker of AD even in its earliest stages. Volumetric analysis of the entorhinal cortex distinguished subjects who were destined to develop dementia from normal controls with high accuracy [32]. However, this approach is time-consuming and highly dependent on analyst expertise because it requires accurate manual outlining of the region of interest for the measurement. Voxel-based morphometry (VBM) has emerged as an ideal tool to visualize the changes in gray matter density in disease states. This technique has been reported to detect gray matter loss in MCI and AD patients. In addition, lower gray matter density has been reported in MCI converters compared with MCI non-converters [33–37]. These findings suggest that measurement of gray matter loss in the medial temporal lobe or the other regions might predict progression from MCI to AD with high accuracy. A direct comparison of MRI with PIB–PET was previously performed in the control, MCI and AD populations [38]. The distributions of hippocampal volume did not overlap between AD and normal control groups with the exception of one control subject, and MCI subjects are evenly distributed between the AD and normal controls. In contrast, PIB–PET uptake showed a bimodal distribution. While all AD subjects are tightly clustered in the high PIB retention range, both the normal control and MCI subjects segregate themselves into high and low PIB retention groups. The voxel-by-voxel comparisons of AD versus control patients revealed differences in the topographical distribution of amyloid deposition and in grey matter loss, suggesting that these two imaging strategies provide complementary information about AD pathology.

In this study, we performed amyloid-imaging PET using [^{11}C]BF-227 and VBM analysis of MRI images in subjects with MCI and AD. We investigated whether changes in BF-227 uptake and gray matter density were associated with later conversion to AD in MCI populations. Moreover, we examined the association of these measurements with cognitive function in AD and MCI converters to investigate whether these imaging strategies can track the severity of AD pathology.

2. Materials and methods

2.1. Staining of senile plaques using BF-227

Postmortem brain tissue from a 69-year-old male with autopsy-confirmed AD was obtained from Fukushimura Hospital (Toyohashi, Japan). Experiments were performed under the regulations of the hospital ethics committee. Serial sections (6 μm) taken from paraffin-embedded blocks of the temporal cortex were prepared in xylene and ethanol. Before BF-227 staining, quenching of autofluorescence was performed. The quenched tissue section was immersed in 100 μM of BF-227 containing 50% ethanol for 10 min. The section stained with BF-227 was then dipped briefly into water and rinsed in PBS for 60 min before coverslipping with FluorSave Reagent (Calbiochem, La Jolla, CA), and examined using an Eclipse E800 microscope (Nikon, Tokyo, Japan) equipped with a V-2A filter set (excitation 380–420 nm, dichroic mirror 430 nm, long pass filter 450 nm). An adjacent section was immunostained using a monoclonal antibody (mAb) against Aβ (6F/3D; Dako A/S, Glostrup, Denmark). After pretreatment with 90% formic acid for 5 min, sections were immersed in blocking solution for 30 min and then incubated for 60 min at 37 °C with 6F/3D at a dilution of 1:50. After incubation, sections were processed with the avidin–biotin method using a Pathostain ABC-POD(M) Kit (Wako, Osaka, Japan) and diaminobenzidine tetrahydrochloride.

2.2. Subjects

Patients recruited in the present study included 12 normal age-matched controls, 13 subjects with amnestic MCI, and 15 patients with AD. Diagnoses of probable AD were based on criteria from the National Institute of Neurological and Communicative Disorders and Stroke and the Alzheimer's Disease Related Disorders Association (NINCDS-ADRDA) [39]. The diagnosis of amnestic MCI was made according to the published criteria described previously [40]. All MCI subjects underwent medical and neuropsychological reevaluation at approximately 3 month intervals. Conversion to AD was diagnosed when (1) signs of deterioration of the general cognitive function were present and continued for at least 6 months, and (2) the patient's score on the Clinical Dementia Rating changed by more than 0.5 points. The MCI subjects were divided into two groups, MCI converters ($n = 6$) and MCI non-converters ($n = 7$). The MCI converters were defined as patients who eventually developed AD within a mean follow-up of 27.0 ± 7.9 months (range 14–30 months). The MCI non-converters were defined as having a transient memory loss or remaining cognitively stable through at least a 2 year follow-up (27.7 ± 2.2 months; range 25–30 months). The control group was recruited from volunteers who were not taking centrally-acting medications, had no cognitive impairment and had no cerebrovascular lesions identified via MRI. All subjects were screened using a questionnaire and medical history, and subjects with medical conditions potentially affecting the central nervous system were excluded. In addition, none

Table 1
Demographic characteristics of the subjects.

	Control	MCI non-converter	MCI converter	AD
N	12	7	6	15
Age (year)	67.3 ± 2.7	77.6 ± 3.1	80.2 ± 4.1	71.0 ± 5.1
Gender (F/M)	6/6	2/5	4/2	8/7
MMSE	29.9 ± 0.3	26.3 ± 1.1	25.7 ± 2.0	19.8 ± 3.5

of the subjects had asymptomatic cerebral infarction detected via T2-weighted MRI. Demographic data for the subjects are shown in Table 1. Although the MCI converters and non-converters were statistically older than the control subjects and the AD patients, no statistical difference in age was observed between the MCI converters and the non-converters. The AD patients showed a significantly lower MMSE score than the MCI converters, non-converters, and control subjects ($p<0.05$), however, no statistical difference in MMSE score was observed between the MCI converters and the non-converters. The Committee on Clinical Investigation at Tohoku University School of Medicine and the Advisory Committee on Radioactive Substances at Tohoku University approved the study protocol.

3. MRI methods

All subjects underwent MRI with a 1.5 T MR scanner (GE Signa Hispeed, Milwaukee, WI). A three-dimensional volumetric acquisition of a T1-weighted gradient echo sequence produced a gapless series of thin axial sections using a vascular TOF SPGR sequence (echo time/repetition time, 2.4/50 ms; flip angle, 45°; acquisition matrix, 256×256; 1 excitation; field of view, 22 cm; slice thickness, 2.0 mm). Cerebral atrophy was evaluated by VBM [41]. For spatial normalization, a 12-parameter affine transformation was used to avoid segmentation errors caused by the partial-volume effects inherently created by warping. The normalized MRI was then segmented into gray matter, white matter, cerebrospinal fluid, and other components using SPM2 or SPM5 software. The segmentation procedure involved calculating the Bayesian probability of each voxel belonging to each tissue class based on a priori MRI information with a non-uniformity correction. The segmented gray matter images were then subjected to affine and non-linear spatial normalization using a template of a priori gray matter. The spatially normalized gray matter images were smoothed with an isotropic Gaussian kernel (12 mm at full width at half maximum) using the partial-volume effects to create a spectrum of gray matter intensities. The resulting gray matter intensities were equivalent to the weighted average of gray matter voxels located in the volume fixed by the smoothing kernel. Regional intensities can thus be considered equivalent to gray matter concentration. Differences of gray matter intensities between groups were assessed using a *t*-test with a height threshold of $p<0.05$, corrected for multiple comparisons by the family-wise error method. The extent threshold was set to 100 voxels. Parahippocampal gray matter density was additionally evaluated by calculating the average intensities in the bilateral parahippocampal region of interest (ROI) using Dr.View/LINUX software (AJS, Japan). To evaluate global atrophy, a *Z*-score map was created via the comparison of individual gray matter images with the mean and S.D. of gray matter images of healthy controls after voxel normalization to global mean intensities. The degree of global atrophy (% global atrophy) was calculated as a ratio of the area in which the *Z*-score of the voxel was more than 2.0 to whole brain area, using Voxel-Based Specific Regional Analysis System for AD (VSRAD) software (Eisai, Tokyo, Japan) [42].

3.1. PET procedure

Radiosynthesis of [^{11}C]BF-227 and the procedure used for BF-227-PET were performed as described previously. [22] BF-227 and its N-desmethylated derivative (a precursor of [^{11}C]BF-227) were custom-synthesized by Tanabe R&D Service Co. [^{11}C]BF-227 was synthesized from its precursor by N-methylation in dimethyl sulfoxide using [^{11}C]methyl triflate. The [^{11}C]BF-227-PET study was performed using a PET SET-2400W scanner (Shimadzu Inc., Japan). After an intravenous injection of 211–366 mBq [^{11}C]BF-227, dynamic PET images were obtained for 60 min with the subject's eyes closed. Standardized uptake value (SUV) images of [^{11}C]BF-227 were obtained by normalizing the tissue radioactivity concentration to the injected dose and body weight. ROIs were placed on individual axial MR images in the cerebellar hemisphere and the frontal, lateral temporal, parietal and posterior cingulate cortices. The ROI information was then copied onto the dynamic PET SUV images, and regional SUVs were sampled using Dr.View/LINUX software. The ratio of the regional to cerebellar SUV (SUVR) at 40–60 min post-injection was calculated, and averaged SUVR values in the frontal, temporal, parietal and posterior cingulate cortices were considered representative of BF-227 retention in the neocortex (neocortical SUVR).

3.2. Statistical analysis

Statistical comparison of PET and MRI measurements in the four groups was performed via an analysis of variance followed by a Bonferroni multiple comparisons test with a significance level of $p<0.05$. Statistical comparisons of age and MMSE scores in the four groups were performed using a Kruskal–Wallis test followed by a Dunn's multiple comparison test with a significance level of $p<0.05$. Correlations between the MMSE score and BF-227 retention in the neocortex or the cerebral atrophy index were examined using a non-parametric Spearman's rank correlation analysis. Correlations between the brain atrophy index and BF-227 retention were determined using Pearson's correlations. A linear model was applied to the data to obtain a correlation coefficient and *p* value. These analyses were performed using GraphPad Prism5 software (GraphPad, San Diego, CA).

4. Results

In order to confirm the selective binding ability of BF-227 to Aβ deposits, neuropathological examination was initially performed using BF-227 staining of AD temporal brain sections. Senile plaques were selectively stained with BF-227 and the staining pattern coincided well with Aβ immunostaining in an adjacent section (Fig. 1). Strikingly, cored plaques were intensely stained with BF-227, indicating preferential BF-227 binding to dense Aβ fibrils. Next,

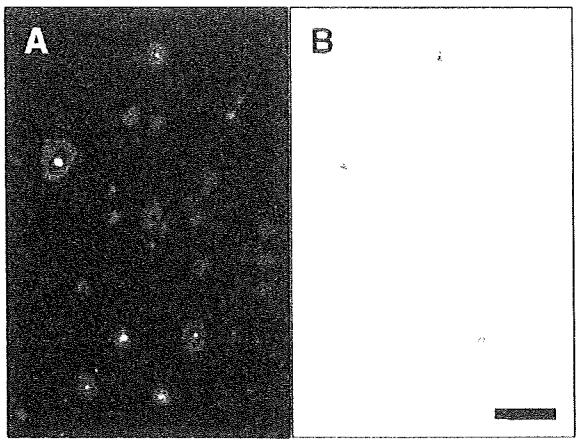

Fig. 1. (A) Neuropathological staining of human brain sections by BF-227. Amyloid plaques are clearly stained with BF-227 in AD temporal brain sections (B) BF-227 staining correlates well with Aβ immunostaining in adjacent sections. Scale bar = 100 μm.

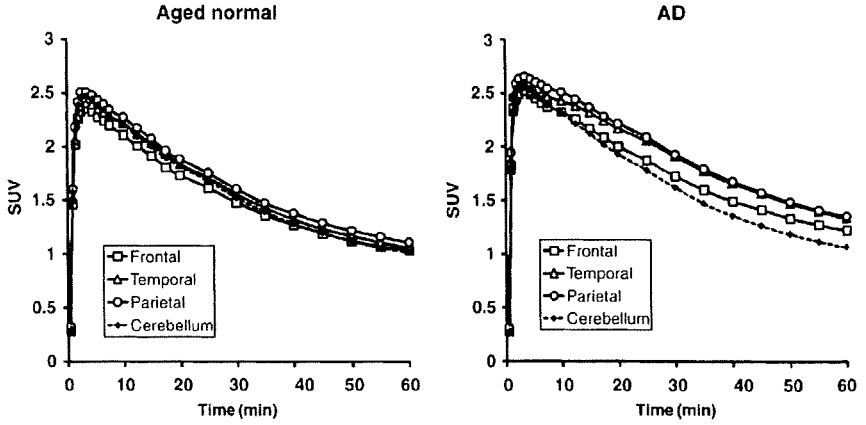

Fig. 2. Tissue time activity data for [^{11}C]BF-227-PET. SUV time activity curves of [^{11}C]BF-227 in the frontal cortex, lateral temporal cortex, parietal cortex and cerebellum are shown. Each point represents the mean of 12 control subjects (left) and 15 AD patients (right).

we performed clinical PET using [^{11}C]BF-227 in AD patients, MCI subjects and control subjects. The tissue time activity curves from [^{11}C]BF-227-PET in 15 AD patients and 12 normal controls are shown in Fig. 2. In AD patients, the frontal, temporal and parietal cortices retained [^{11}C]BF-227 to a greater extent at later time points, compared with controls. AD patients showed significantly higher SUVs in the temporal cortex and average neocortex than controls, but not in the cerebellum (Table 2). Therefore, neocortical SUV elevation in AD patients presumably reflects the specific binding of BF-227 to amyloid plaques. Representative images of [^{11}C]BF-227-PET and T1-weighted MRI in a normal control (70-year-old female, MMSE score 29), a MCI non-converter (76-year-old male, MMSE score 27), a MCI converter (85-year-old male, MMSE score 23), and an AD patient (62-year-old female, MMSE score 20) are shown in Fig. 3. Increased BF-227 retention was evident in both the MCI converter and the AD patient, but not in the control subject or the MCI non-converter. In AD patients, BF-227 SUVRs in the frontal, temporal, parietal and posterior cingulate cortices were significantly higher compared to the control subjects and the MCI non-converters (Table 2). A significant elevation of BF-227 SUVR was additionally observed in the frontal, temporal and parietal cortices of MCI converters compared with the control subjects. Consequently, the average neocortical SUVR was significantly higher in the AD patients and MCI converters than in normal subjects and MCI non-converters (Table 2). When a neocortical BF-227 SUVR of 1.11 (1.5SD above control mean) was used as a cut-off, sensitivity of 100% and a specificity of 91.7% in the discrimination between AD patients and normal subjects were achieved.

The voxel-based comparison of gray matter images using SPM5 demonstrated a significant decline of gray matter concentrations in the left ($-28, 14, -26, x, y, z; Z = 5.26$) and the right ($32, 18, -26, x, y, z; Z = 5.24$) medial temporal cortices of AD patients, compared with control subjects (Fig. 4A). SPM2 analysis using the same samples also showed a reduction of gray matter concentrations in nearly the same region and significance (data not shown). We drew the ROI in the parahippocampal area (Fig. 4B) and performed a comparison between the four groups. Significantly lower gray matter intensity was observed in the AD patients, MCI converters and MCI non-converters than in controls (Table 2, Fig. 5). However, age-related changes may be a confounding factor resulting in lower gray matter intensity in MCI groups, as MCI subjects were older than the normal control group. When a parahippocampal ROI value from SPM5 of 0.537 (2SD below control mean) was used as a cut-off, a sensitivity of 80.0% and a specificity of 100% were achieved in the discrimination between AD patients and normal subjects. No significant inter-group difference was observed in the percent global atrophy in VBM analysis due to substantial differences between individuals.

We focused on the comparison between the MCI converters and the non-converters, because these two populations showed no significant difference in age or MMSE scores. A significant inter-group difference was observed in the frontal and the average neocortical SUVR assayed by BF-227-PET, but not in the percent global atrophy or parahippocampal ROI value obtained by VBM-MRI (Table 2, Fig. 5). However, MCI converters showed a tendency toward lower parahippocampal ROI value derived from SPM5 than MCI non-converters.

Table 2
Summary of imaging measures.

	Normal	MCI non-converter	MCI converter	AD
BF-227 SUV in cerebellum	1.10 ± 0.19	1.08 ± 0.17	1.16 ± 0.22	1.16 ± 0.16
BF-227 SUV in frontal cortex	1.11 ± 0.19	1.10 ± 0.16	1.36 ± 0.33	1.31 ± 0.22
BF-227 SUV in temporal cortex	1.14 ± 0.19	1.19 ± 0.18	1.39 ± 0.28	1.45 ± 0.24[a]
BF-227 SUV in parietal cortex	1.20 ± 0.21	1.20 ± 0.18	1.38 ± 0.29	1.46 ± 0.23
BF-227 SUV in posterior cingulate cortex	1.22 ± 0.22	1.23 ± 0.22	1.39 ± 0.27	1.47 ± 0.21
Average neocortical BF-227 SUV	1.17 ± 0.20	1.18 ± 0.18	1.38 ± 0.29	1.42 ± 0.22[a]
BF-227 SUVR in frontal cortex	1.01 ± 0.06	1.02 ± 0.07	1.16 ± 0.10[a,b]	1.13 ± 0.08[a,b]
BF-227 SUVR in temporal cortex	1.04 ± 0.04	1.10 ± 0.07	1.20 ± 0.07[a]	1.24 ± 0.08[a,b]
BF-227 SUVR in parietal cortex	1.09 ± 0.04	1.12 ± 0.05	1.18 ± 0.07[a]	1.25 ± 0.08[a,b]
BF-227 SUVR in posterior cingulate cortex	1.11 ± 0.06	1.14 ± 0.07	1.20 ± 0.09	1.26 ± 0.05[a,b]
Average neocortical BF-227 SUVR	1.06 ± 0.04	1.09 ± 0.06	1.19 ± 0.07[a,b]	1.22 ± 0.06[a,b]
Percent global atrophy in VBM-MRI	4.24 ± 3.49	7.35 ± 5.94	5.96 ± 3.06	8.53 ± 4.44
Parahippocampal ROI value in VBM-MRI (SPM2)	0.642 ± 0.034	0.569 ± 0.039[a]	0.553 ± 0.044[a]	0.541 ± 0.055[a]
Parahippocampal ROI value in VBM-MRI (SPM5)	0.605 ± 0.034	0.510 ± 0.051[a]	0.473 ± 0.060[a]	0.475 ± 0.068[a]

[a] $p < 0.05$ vs. aged normal.
[b] $p < 0.05$ vs. MCI non-converter.

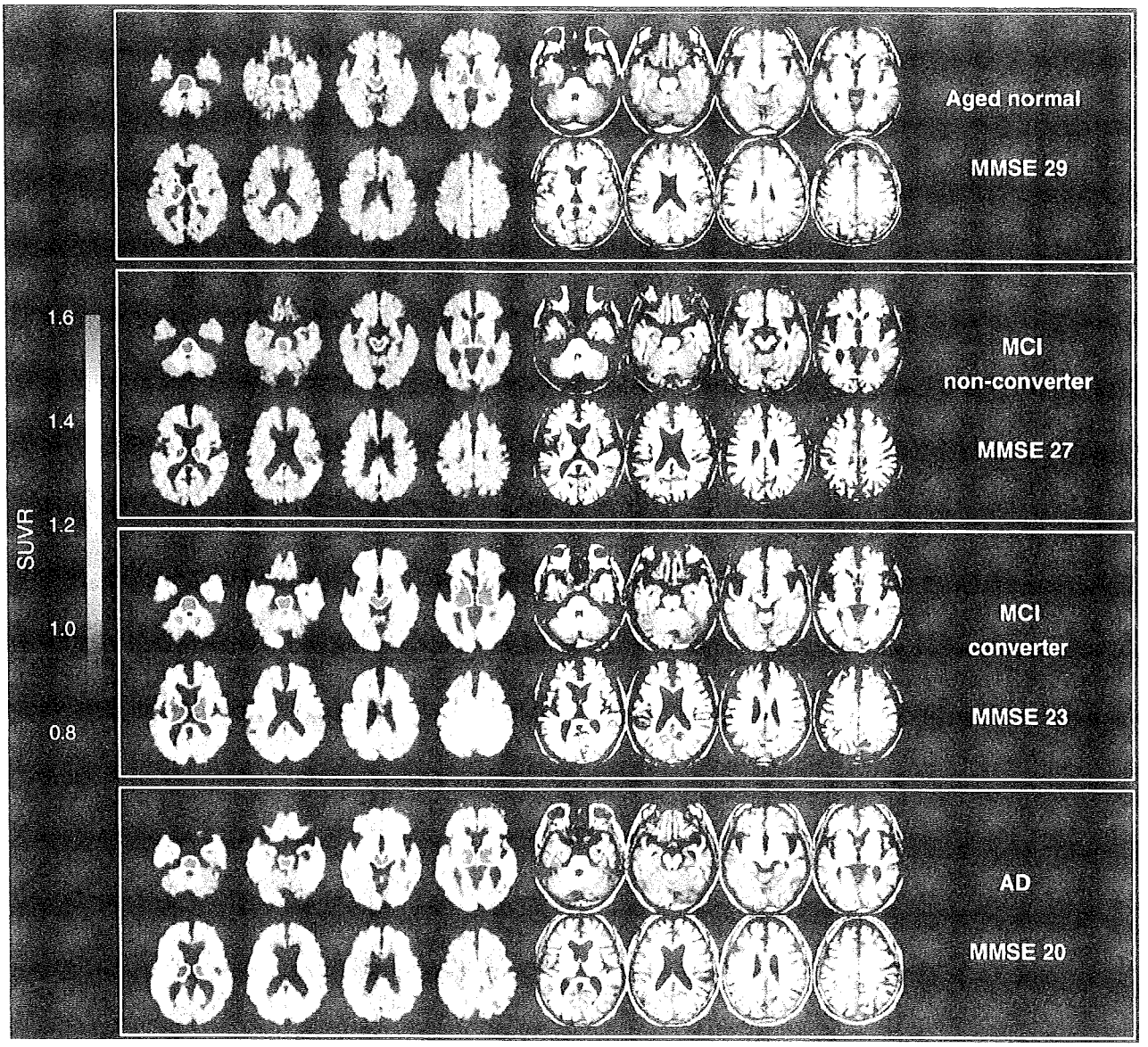

Fig. 3. Representative images of [^{11}C]BF-227–PET SUVR between 20 and 40 min post-injection (left) and T1-weighted MRI (right) in a control subject, a MCI non-converter, a MCI converter and an AD subject. The degree of [^{11}C]BF-227 retention is shown by color intensity from yellow to red in the cortex.

When we used a neocortical BF-227 SUVR of 1.11 as a cut-off, we achieved a sensitivity of 100% and a specificity of 71.4% in the discrimination between MCI converters and the MCI non-converters. These values were superior to the results of the parahippocampal ROI value derived from SPM5 (cut-off value: 0.537), which showed a sensitivity of 83.3% and a specificity of 42.9%. These data suggest that BF-227–PET is a better predictor of conversion from MCI to AD than VBM–MRI.

Next, we examined the correlations between MMSE scores and the three volume measurements (Fig. 6). When all subjects ($N=40$) were included in this analysis, a significant negative correlation was observed in all three measurements (BF-227 SUVR $r=-0.740$, $p<0.001$; percent global atrophy $r=-0.491$, $p=0.001$; parahippocampal ROI from SPM2 $r=0.674$, $p<0.001$; and parahippocampal ROI from SPM5 $r=0.687$, $p<0.001$). However, when we confined the analysis to the combined group of AD patients and MCI converters, we observed a significant correlation only between the percent global atrophy and the MMSE score (Spearman $r=-0.459$, $p=0.036$). In contrast, no significant correlation was observed between the parahippocampal ROI from SPM2 and the MMSE (Spearman $r=0.192$), between the parahippocampal ROI from SPM5 and the MMSE (Spearman $r=0.181$) or between the BF-227 SUVR in the neocortex and the MMSE (Spearman $r=-0.200$). Finally, no significant correlation was observed between the BF-227 SUVR and the percent global atrophy or parahippocampal atrophy in the analysis of all subjects.

5. Discussion

In the present study, MCI converters were more clearly distinguished from MCI non-converters by BF-227–PET than by VBM–MRI. The MCI non-converters showed a normal distribution of BF-227 except for one case, but also showed lower gray matter density in the parahippocampal gyrus than did normal controls. As a result, BF-227–PET achieved higher sensitivity and specificity in the discrimination between MCI converters and MCI non-converters than did VBM–MRI.

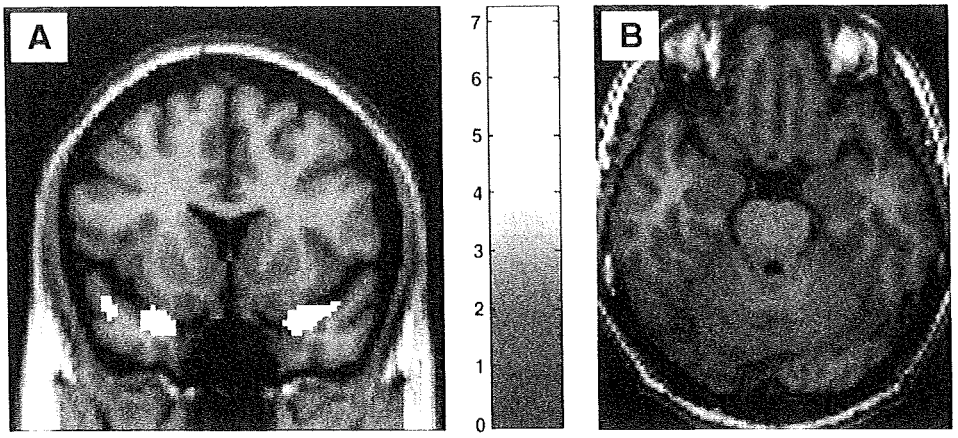

Fig. 4. (A) Areas of reduction in gray matter density of AD patients compared with aged normal controls. $p<0.05$, corrected for multiple comparisons. Left in the image is left in the brain. Color bars represent T values. (B) Regions of interest within the parahippocampal gyrus.

Our results strongly suggest that amyloid imaging using BF-227-PET will be a useful tool to predict conversion from MCI to AD, as previously shown for PIB-PET. [17,18] However, cerebral gray matter loss as determined by VBM-MRI was better correlated with the clinical severity of AD than BF-227-PET. Used together, BF-227-PET and VBM-MRI could be an effective method for the early diagnosis and severity tracking of AD. Our findings may be compatible with the theory that amyloid deposition reaches equilibrium or plateaus at an early stage of AD, making in vivo amyloid imaging useful in the examination of pre-symptomatic subjects [15,16]. Aβ deposition is a pathological hallmark of AD, but may also occur in normal elderly individuals who do not exhibit apparent cognitive decline. In fact, a PIB-PET study showed that 22% of healthy elderly individuals showed increased cortical PIB binding, indicating the presence of Aβ plaques in these non-symptomatic subjects [15]. A strong relationship between the impairment of episodic memory and PIB binding has also been shown both in subjects with MCI and in the normal population, suggesting that individuals with increased cortical PIB

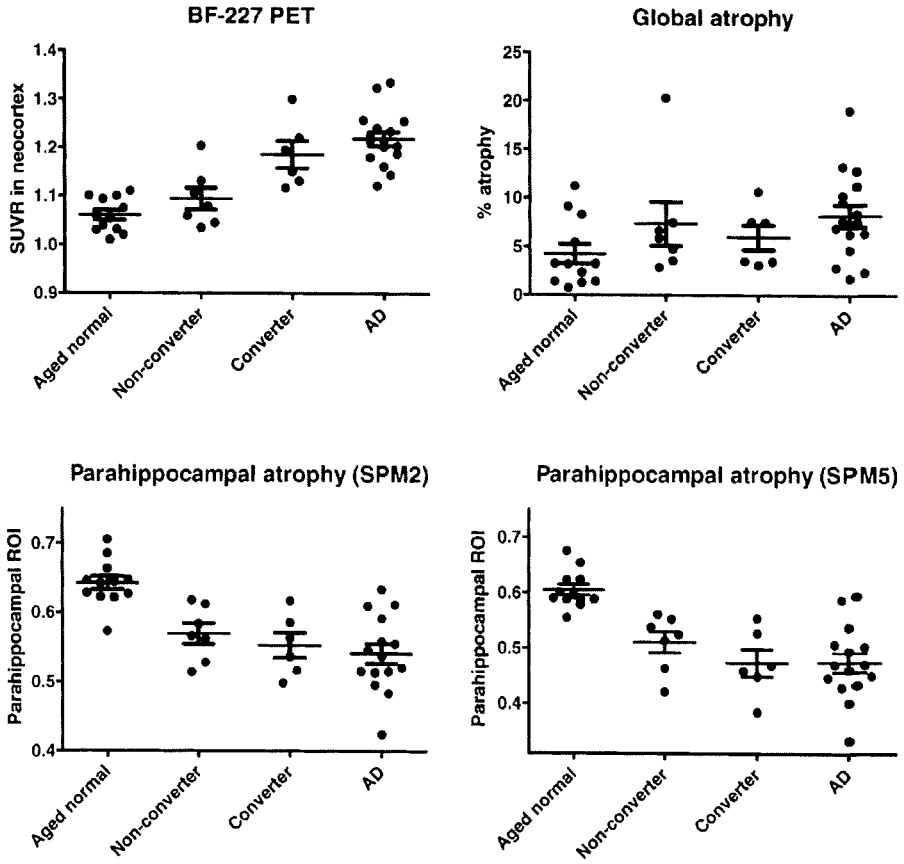

Fig. 5. Comparison of BF-227 SUVR in the neocortex (upper left), the percent global atrophy (upper right), the parahippocampal region of interest (ROI) value from gray matter images processed by SPM2 (lower left) and the parahippocampal ROI value from gray matter images processed by SPM5 (lower right) in control subjects, MCI non-converters, converters and AD patients.

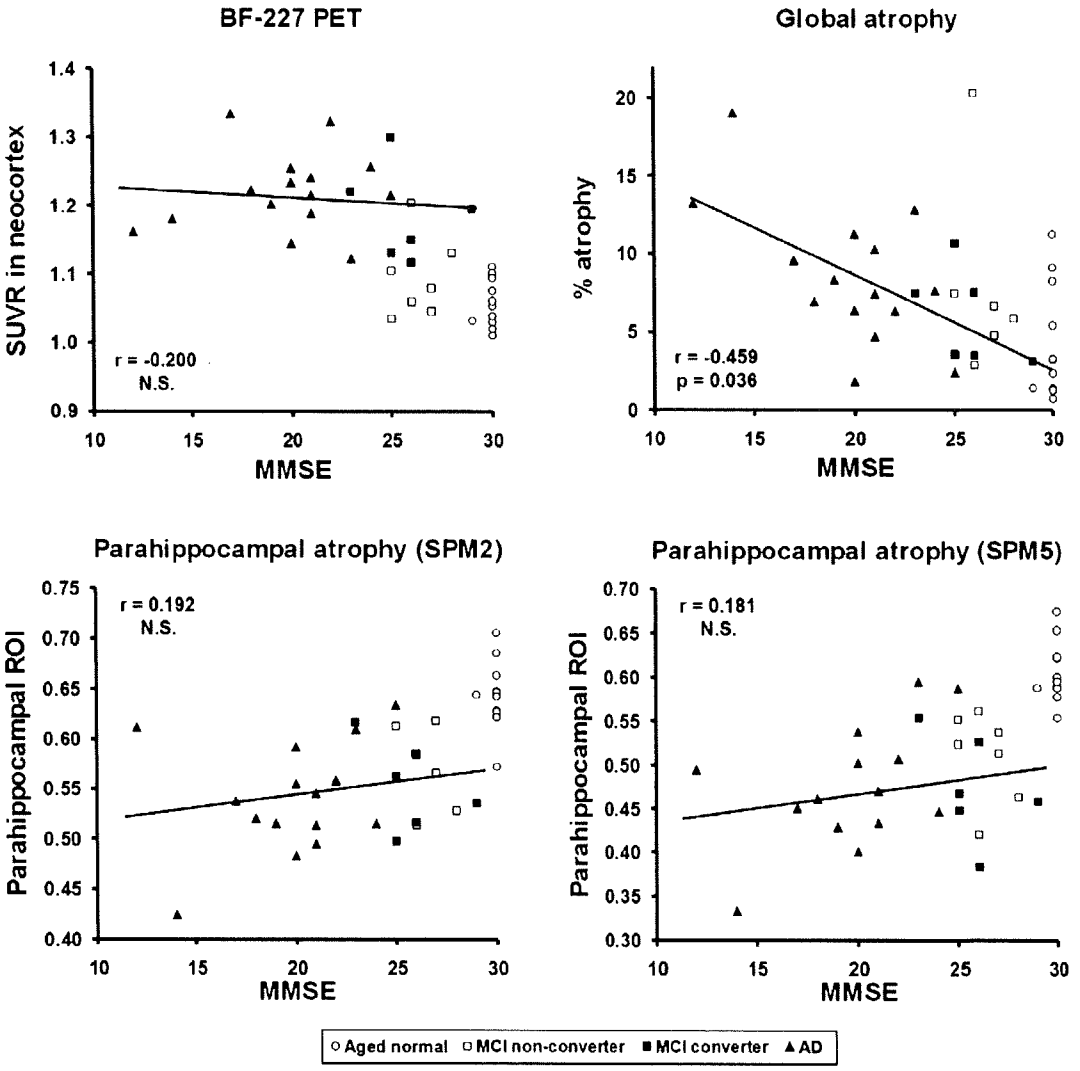

Fig. 6. The correlations of MMSE scores with the BF-227 SUVR in the neocortex (upper left), the percent global atrophy (upper right), the parahippocampal region of interest (ROI) value from gray matter images processed by SPM2 (lower left), and the parahippocampal ROI value from gray matter images processed by SPM5 (lower right). Open circle: control; open square: MCI non-converter; filled square: MCI converter; filled triangle: AD.

binding are proceeding to AD [43]. In our study, almost all normal subjects exhibited a normal distribution of BF-227 in the brain. This finding may suggest a lower sensitivity of diffuse amyloid plaque detection by BF-227 [22]. However, the proportion of amyloid PET-positive individuals in the normal population varies greatly depending on the characteristics of the sample population. Indeed, the mean age of the control subjects in our study was somewhat younger than in previous PIB–PET studies. Therefore, a direct comparison of BF-227–PET with PIB–PET in the same normal population is necessary to compare the ability of these agents to detect early AD pathology. A longitudinal follow-up of amyloid PET-positive cases in the healthy, normal population will also elucidate whether tracer uptake reflects pre-symptomatic detection of AD or a false-positive finding. A follow-up study of the patients with AD using PIB–PET showed that the amyloid deposition remains high but stable, despite decreases in regional glucose metabolism and cognitive function.[44] Our cross-sectional analysis also revealed a plateau of cortical BF-227 uptake in early AD patients, suggesting that amyloid formation reaches a plateau early in the course of AD. A potential limitation of this study is that it used a semiquantitative SUV measure to estimate BF-227 binding to amyloid plaques. The levels of neocortical BF-227 SUV might be underestimated due to hypoperfusion in AD patients. Quantitative analysis should be performed in future analyses to eliminate the influence of blood flow change.

A previous PIB–PET study found a positive correlation between the rate of whole brain atrophy and amyloid plaque load. [45] However, a recent PET study discovered a discrepancy between regional PIB retention and gray matter loss [38]. Additionally, histopathological analysis revealed no association between Aβ burden and brain atrophy [46]. The present study also found no significant correlation between neocortical BF-227 uptake and global gray matter loss in AD patients, in agreement with these findings. In our correlation analysis of the four measurements with the MMSE scores, we confined our analysis to AD patients and MCI converters because these patients share the same pathological process underlying AD. Therefore, this is more appropriate for the correlation analysis between cognitive function and the degree of Aβ burden or cerebral atrophy induced by the pathological process of AD than an analysis using all samples, including the normal population. In this analysis, the global gray matter loss measured by VBM–MRI was better correlated with MMSE scores than was the Aβ burden measured by BF-227–PET. A similar correlation analysis performed using PIB–PET demonstrated that the

magnitudes of the correlations were greater for hippocampal atrophy than for neocortical PIB retention [38]. The current result, showing no significant correlation of the parahippocampal gray matter density with the MMSE score, seems to be inconsistent with previous PIB–PET data. We believe this discrepancy to be due mainly to differences in the sample population. The analysis in the previous PIB–PET study was performed using all the subjects, including the normal controls; our analysis was confined to AD patients and MCI converters who had already developed severe memory decline and probably substantial neuron loss in the hippocampus. These results suggest that global, rather than parahippocampal, gray matter loss is a potent indicator of dementia severity after the onset of memory loss in AD. We hope to explore the relationship between these imaging measurements and the impairment of episodic memory function in a future study.

It has been reported that the degree or rate of change of cerebral atrophy as measured by MRI analysis is closely related to the clinical progression of dementia [29,30]. Karas et al. performed a VBM–MRI analysis to examine the global and regional gray matter loss in normal, MCI and AD subjects, finding a significantly lower global gray matter volume in the AD subjects and an intermediate volume in the MCI subjects [31]. They followed the MCI subjects and observed greater gray matter loss in the MCI converters than in non-converters [37]. Another study also revealed different patterns of gray matter density distribution between MCI converters and non-converters [35]. From these findings, it appears that gray matter loss in VBM is a good indicator of conversion from MCI to AD. We failed to demonstrate significant inter-group differences between the MCI converters and non-converters, although the MCI converters showed a tendency toward lower parahippocampal gray matter density than did the non-converters. This, however, may be due to the small sample size and insufficient follow-up period (over two years) of the MCI subjects in this study. For example, one MCI non-converter in our study showed an abnormality in both the BF-227 SUVR and parahippocampal gray matter density; extending the follow-up period of the MCI subjects would likely result in more consistent correlation between MCI conversion to AD and the described measurements. Additional longitudinal studies are also needed to confirm the findings we have obtained and to examine the time course of AD, including changes in the pre-symptomatic subjects, and to determine the relationship between amyloid deposition and brain atrophy as underlying factors in the pathogenesis of AD.

Acknowledgements

We appreciate the technical assistance of Dr. S. Watanuki, Dr. Y. Ishikawa, Dr. M. Mori, and Dr. K. Sugi in the clinical PET studies and the support of Fukushimura Hospital for the histochemical studies. We also thank to Dr. H. Akatsu and Dr. T. Yamamoto for supplying brain samples. This study was supported by the Program for the Promotion of Fundamental Studies in Health Science of the National Institute of Biomedical Innovation, the Industrial Technology Research Grant Program in 2004 of the New Energy and Industrial Technology Development Organization (NEDO) of Japan, Health and Labor Sciences Research Grants for Translational Research from the Ministry of Health, an Asan Trazeneca Research Grant, and the Novartis Foundation for Gerontological Research.

References

[1] Blennow K, de Leon MJ, Zetterberg H. Alzheimer's disease. Lancet 2006;368: 387–403.
[2] Drachman DA. Aging of the brain, entropy, and Alzheimer disease. Neurology 2006;67:1340–52.
[3] Braak H, Braak E. Neuropathological stageing of Alzheimer-related changes. Acta Neuropathol 1991;82:239–59.
[4] Arnold SE, Hyman BT, Flory J, Damasio AR, Van Hoesen GW. The topographical and neuroanatomical distribution of neurofibrillary tangles and neuritic plaques in the cerebral cortex of patients with Alzheimer's disease. Cereb Cortex 1991;1:103–16.
[5] Mouton PR, Martin LJ, Calhoun ME, Dal Forno G, Price DL. Cognitive decline strongly correlates with cortical atrophy in Alzheimer's dementia. Neurobiol Aging 1998;19:371–7.
[6] Masters CL, Cappai R, Barnham KJ, Villemagne VL. Molecular mechanisms for Alzheimer's disease: implications for neuroimaging and therapeutics. J Neurochem 2006;97:1700–25.
[7] Nordberg A. PET imaging of amyloid in Alzheimer's disease. Lancet Neurol 2004;3: 519–27.
[8] Villemagne VL, Rowe CC, Macfarlane S, Novakovic KE, Masters CL. Imaginem oblivionis: the prospects of neuroimaging for early detection of Alzheimer's disease. J Clin Neurosci 2005;12:221–30.
[9] Mathis CA, Klunk WE, Price JC, DeKosky ST. Imaging technology for neurodegenerative diseases: progress toward detection of specific pathologies. Arch Neurol 2005;62:196–200.
[10] Nordberg A. Amyloid imaging in Alzheimer's disease. Curr Opin Neurol 2007;20: 398–402.
[11] Small GW, Kepe V, Ercoli LM, Siddarth P, Bookheimer SY, Miller KJ, et al. PET of brain amyloid and tau in mild cognitive impairment. N Engl J Med 2006;355:2652–63.
[12] Klunk WE, Engler H, Nordberg A, Wang Y, Blomqvist G, Holt DP, et al. Imaging brain amyloid in Alzheimer's disease with Pittsburgh Compound-B. Ann Neurol 2004;55:306–19.
[13] Price JC, Klunk WE, Lopresti BJ, Lu X, Hoge JA, Ziolko SK, et al. Kinetic modeling of amyloid binding in humans using PET imaging and Pittsburgh Compound-B. J Cereb Blood Flow Metab 2005;25:1528–47.
[14] Lopresti BJ, Klunk WE, Mathis CA, Hoge JA, Ziolko SK, Lu X, et al. Simplified quantification of Pittsburgh Compound B amyloid imaging PET studies: a comparative analysis. J Nucl Med 2005;46:1959–72.
[15] Rowe CC, Ng S, Ackermann U, Gong SJ, Pike K, Savage G, et al. Imaging beta-amyloid burden in aging and dementia. Neurology 2007;68:1718–25.
[16] Mintun MA, Larossa GN, Sheline YI, Dence CS, Lee SY, Mach RH, et al. [^{11}C]PIB in a nondemented population: potential antecedent marker of Alzheimer disease. Neurology 2006;67:446–52.
[17] Fripp J, Bourgeat P, Acosta O, Raniga P, Modat M, Pike KE, et al. Appearance modeling of ^{11}C PiB PET images: characterizing amyloid deposition in Alzheimer's disease, mild cognitive impairment and healthy aging. Neuroimage 2008;43:430–9.
[18] Forsberg A, Engler H, Almkvist O, Blomquist G, Hagman G, Wall A, et al. PET imaging of amyloid deposition in patients with mild cognitive impairment. Neurobiol Aging 2008;29:1456–65.
[19] Okamura N, Suemoto T, Shimadzu H, Suzuki M, Shiomitsu T, Akatsu H, et al. Styrylbenzoxazole derivatives for in vivo imaging of amyloid plaques in the brain. J Neurosci, 2004;24:2535–41.
[20] Okamura N, Furumoto S, Funaki Y, Suemoto T, Kato M, Ishikawa Y, et al. Binding and safety profile of novel benzoxazole derivative for in vivo imaging of amyloid deposits in Alzheimer's disease. Geriatr Gerontol Int 2007;7:393–400.
[21] Furumoto S, Okamura N, Iwata R, Yanai K, Arai H, Kudo Y. Recent advances in the development of amyloid imaging agents. Curr Top Med Chem 2007;7:1773–89.
[22] Kudo Y, Okamura N, Furumoto S, Tashiro M, Furukawa K, Maruyama M, et al. 2-(2-[2-Dimethylaminothiazol-5-yl]Ethenyl)-6-(2-[Fluoro]Ethoxy)Benzoxazole: A novel PET agent for in vivo detection of dense amyloid plaques in Alzheimer's disease patients. J Nucl Med 2007;48:553–61.
[23] Fodero-Tavoletti MT, Mulligan RS, Okamura N, Furumoto S, Rowe CC, Kudo Y, et al. In vitro characterization of BF227 binding to α-synuclein/Lewy Bodies. Eur J Pharmacol 2009;617:54–8.
[24] Ishii K, Hashimoto M, Kimura Y, Sakata M, Oda K, Kawasaki K, et al. Direct comparison of in vivo accumulation of ^{11}C-PIB and ^{11}C-BF227 in Alzheimer's disease. Alzheimer's and Dementia, vol. 4, Issue 4; July 2008. p. T49. Supplement 1.
[25] Tiraboschi P, Hansen LA, Thal LJ, Corey-Bloom J. The importance of neuritic plaques and tangles to the development and evolution of AD. Neurology 2004;62:1984–9.
[26] Price JL, Morris JC. Tangles and plaques in nondemented aging and "preclinical" Alzheimer's disease. Ann Neurol 1999;45:358–68.
[27] Morris JC, Storandt M, Miller JP, McKeel DW, Price JL, Rubin EH, et al. Mild cognitive impairment represents early-stage Alzheimer disease. Arch Neurol 2001;58:397–405.
[28] Wang J, Dickson DW, Trojanowski JQ, Lee VM. The levels of soluble versus insoluble brain Abeta distinguish Alzheimer's disease from normal and pathologic aging. Exp Neurol 1999;158:328–37.
[29] Fox NC, Crum WR, Scahill RI, Stevens JM, Janssen JC, Rossor MN. Imaging of onset and progression of Alzheimer's disease with voxel-compression mapping of serial magnetic resonance images. Lancet 2001;358:201–5.
[30] Jack Jr CR, Shiung MM, Gunter JL, O'Brien PC, Weigand SD, Knopman DS, et al. Comparison of different MRI brain atrophy rate measures with clinical disease progression in AD. Neurology 2004;62:591–600.
[31] Karas GB, Scheltens P, Rombouts SA, Visser PJ, van Schijndel RA, Fox NC, et al. Global and local gray matter loss in mild cognitive impairment and Alzheimer's disease. Neuroimage 2004;23:708–16.
[32] Killiany RJ, Gomez-Isla T, Moss M, Kikinis R, Sandor T, Jolesz F, et al. Use of structural magnetic resonance imaging to predict who will get Alzheimer's disease. Ann Neurol 2000;47:430–9.
[33] Bell-McGinty S, Lopez OL, Meltzer CC, Scanlon JM, Whyte EM, Dekosky ST, et al. Differential cortical atrophy in subgroups of mild cognitive impairment. Arch Neurol 2005;62:1393–7.
[34] Chetelat G, Landeau B, Eustache F, Mezenge F, Viader F, de la Sayette V, et al. Using voxel-based morphometry to map the structural changes associated with rapid conversion in MCI: a longitudinal MRI study. Neuroimage 2005;27:934–46.
[35] Bozzali M, Filippi M, Magnani G, Cercignani M, Franceschi M, Schiatti E, et al. The contribution of voxel-based morphometry in staging patients with mild cognitive impairment. Neurology 2006;67:453–60.